Tropical Cyclone Boundary Layer Asymmetries in a Tilt-Following Perspective

CHAU-LAM YU,[a] BRIAN TANG,[a] AND ROBERT G. FOVELL[a]

[a] *Department of Atmospheric and Environmental Sciences, University at Albany, State University of New York, Albany, New York*

(Manuscript received 29 September 2023, in final form 29 May 2024, accepted 24 June 2024)

ABSTRACT: Previous observations and modeling studies showed that tropical cyclones (TCs) in a sheared environment develop an asymmetric boundary layer (BL). While the relationship between the BL asymmetries and environmental shear has been demonstrated, the exact cause of these BL asymmetries and the phase relationship between them are less well understood. In this study, we examine the dynamical processes leading to the asymmetric structure of the TC BL in a sheared environment using idealized, convection-permitting model simulations. Our results show that the emergence of the BL asymmetries is closely linked to the TC vortex tilt and rainband processes. Specifically, stratiform diabatic processes in the downtilt-left region result in midlevel descending inflow, which brings midtropospheric, low-θ_E air toward the BL and forms a surface cold pool in the downtilt-left quadrant. This descending inflow also advects high absolute angular momentum inward, redistributing the vertical vorticity and causing a storm-scale tangential wind acceleration within the downtilt-left quadrant. As the BL low-θ_E air advances inward, it becomes supergradient and decelerates radially, forming BL outflow in the uptilt-left quadrant. The outflow advects positive relative vorticity uptilt, forming an elliptic BL vorticity and circulation structure. As the tilted TC vortex and the accompanying rainband precess cyclonically over time, the above sequence of events and the resultant BL asymmetries also precess cyclonically, maintaining a quasi-stationary configuration relative to the vortex tilt. These results suggest that the primary organizing factor of the boundary layer asymmetries is the tilted vortex structure and not strictly the environmental shear direction.

KEYWORDS: Mesoscale processes; Wind shear; Boundary layer; Tropical cyclones

1. Introduction

The boundary layer (BL) is an essential part of tropical cyclones (TCs), where enthalpy uptake through sensible and latent heat fluxes and inward transport of absolute angular momentum occur. While the TC BL is typically dominated by frictional convergence and radial inflow, it often exhibits an asymmetric structure, such as in the presence of environmental vertical wind shear (VWS) (Zhang et al. 2013; DeHart et al. 2014; Gu et al. 2016; Nguyen and Molinari 2015; Klotz and Jiang 2017; Ahern et al. 2021; Alland and Davis 2022; Wadler et al. 2022), storm motion (Shapiro 1983; Thomsen et al. 2015; Kepert 2001; Kepert and Wang 2001; Williams 2023), and proximity of land (Barnes and Dolling 2013; Williams 2023; Hlywiak and Nolan 2022). Due to the significant impacts of VWS on TC vortex structure and the distribution of convection and precipitation (Corbosiero and Molinari 2002; DeMaria 1996; Rios-Berrios et al. 2018), TC BL asymmetries have been mainly analyzed in a shear-relative perspective (Zhang et al. 2013; Molinari and Vollaro 2010; Molinari et al. 2012; Wadler et al. 2018a,b, 2022). However, besides VWS, our understanding of the underlying mechanisms of the BL asymmetries and their connection with the TC structure is incomplete. Given the complex interplay between BL processes, TC vortex structure, and environmental VWS, efforts to better understand the impacts of TC BL asymmetries on the structure and intensity evolution of TCs are important to advance our comprehension of the diversity of TC behaviors in sheared environments.

TC BL asymmetric structure was analyzed by Zhang et al. (2013) using dropsonde data in a shear-relative composite framework. They showed that sheared TCs have deep inflow in the downshear quadrants, with the strongest inflow in the downshear-left (DSL) quadrant. While upshear, there is a weaker and shallower inflow layer situated underneath an outflow layer near the BL top at 1.5 km. The tangential wind asymmetry, on the other hand, has an azimuthal phase shift from that of the radial velocity asymmetry, with the strongest tangential wind left of shear and the weakest tangential wind right of shear. Additionally, there is a negative equivalent potential temperature θ_E anomaly over the left-of-shear half of the TC inner core and a positive θ_E anomaly over the right-of-shear half. Similar shear-relative, asymmetric BL structures have been identified by other observational studies (Wadler et al. 2018a,b, 2022; Ming et al. 2014, 2015; Molinari and Vollaro 2010; Molinari et al. 2012) and modeling studies (Ahern et al. 2021; Alland and Davis 2022; Alland et al. 2021a,b; Gu et al. 2015, 2016; Riemer et al. 2010; Riemer 2016; Li and Dai 2020; Dai et al. 2023). While many of these studies examined the potential effects of these asymmetries on the intensity evolution of TCs, it is not clear how these asymmetries develop and are related to other elements of the TC structure.

VWS exerts significant influence not only on the structure of the TC BL but also on the overall vertical structure of the TC vortex, as documented in numerous studies (Black et al. 2002; Corbosiero and Molinari 2002; Riemer et al. 2010; Reasor et al. 2013; Rogers et al. 2013; DeHart et al. 2014; Nguyen et al. 2017; Rios-Berrios et al. 2018; Ryglicki et al. 2018). In a sufficiently sheared environment, a TC becomes vertically tilted, which imposes an asymmetric vorticity distribution above the TC BL, forcing enhanced boundary layer

Corresponding author: Chau-Lam Yu, cyu7@albany.edu

DOI: 10.1175/JAS-D-23-0178.1

TABLE 1. Parameterization schemes used in the CM1 simulation.

Categories	Parameterization schemes	References
Microphysics	Morrison double moment	Bryan and Morrison (2012)
Radiation	RRTMG longwave and shortwave	Iacono et al. (2008)
PBL	Louis	Hong et al. (2006)
Surface fluxes	Bulk aerodynamic formulas	Fairall et al. (2003), Donelan et al. (2004), Drennan et al. (2007)

frictional convergence and ascent downshear (Reasor et al. 2013; Riemer 2016; Schecter 2022). Meanwhile, the misaligned vortex also induces an asymmetric warm anomaly uptilt and cold anomaly downtilt (Raymond 1992; Jones 1995). Descent suppresses convection uptilt, and ascent enhances convection downtilt (Raymond 1992; Jones 1995; Boehm and Bell 2021; Rios-Berrios et al. 2024). The result is a wavenumber-1 asymmetry in the convection distribution (Reasor et al. 2000; Corbosiero and Molinari 2002; Chen et al. 2006; Reasor and Eastin 2012; DeMaria 1996; Wang and Holland 1996; Frank and Ritchie 2001).

The TC vortex tilt tends to cyclonically precess (Tao and Zhang 2014; Rios-Berrios et al. 2018; Rios-Berrios 2020; Rios-Berrios et al. 2024; Yu et al. 2023a,b). During vortex precession, the tilted vortex and rainband convection propagate cyclonically from the downshear-left quadrant toward the upshear-left (USL) quadrant, which typically precedes vortex alignment and intensification (Tao and Zhang 2014; Chen and Gopalakrishnan 2015; Nguyen and Molinari 2015; Gu et al. 2019; Chen et al. 2019; Gopalakrishnan et al. 2019; Wadler et al. 2021; Rios-Berrios et al. 2018; Rios-Berrios 2020; Rios-Berrios et al. 2024; Yu et al. 2023a,b). As the vortex precession proceeds, TC BL asymmetries are also continuously modulated by tilt-influenced, mesoscale processes.

One such process is the downward flux of low-θ_E air, or downdraft ventilation, into the BL in rainbands (Tang and Emanuel 2012a; Powell 1990; Hence and Houze 2008; Didlake and Houze 2009; Riemer et al. 2010, 2013; Bhalachandran et al. 2019; Alland et al. 2021a; Wadler et al. 2021). This downdraft ventilation results in a negative BL θ_E anomaly left of shear, which could negatively affect intensity (Tang and Emanuel 2012b; Riemer et al. 2013; Smith and Montgomery 2015; Gao et al. 2017; Alland and Davis 2022). The convective structure and location of rainbands where downdraft ventilation occurs are likewise influenced by the tilt. Riemer (2016) showed that the stationary rainband complex structure and location are a consequence of asymmetric frictional convergence due to the tilt and the distortion of the low-level moist envelope. Using both dry and moist, idealized simulations, Gu et al. (2018, 2019) showed that the BL inflow and anomalous upward motions are tightly locked with vortex tilt, which is the consequence of the balanced response to the tilted vortex structure, not to the deep-layer shear. Their findings suggest that vortex tilt plays the dominant role in determining the vortex-scale asymmetries. A reasonable question to pose is then to what degree are BL θ_E asymmetries, and other asymmetries in kinematic fields, tied to the vortex tilt.

While the association between the observed boundary layer kinematic and thermodynamic asymmetries and the environmental shear has been demonstrated in previous studies, the driving mechanisms of the structural evolution of these asymmetries are less understood. For instance, what are the physical processes and driving mechanisms that link the wind field and thermodynamic asymmetries? Is there a physical connection between the azimuthal phase relationship of asymmetries in the radial velocity, tangential wind, and θ_E? What is the role of the vortex tilt in the evolution of boundary layer asymmetries? In this study, we investigate these questions by examining the evolution of the boundary layer asymmetries in an idealized model simulation, with a particular focus on the sequence of events that leads to the boundary layer asymmetric structure. Our focus will be on a TC simulation in moderate shear, but we will address the sensitivity of our results to other simulation choices later in the paper. Our overall goal is to gain a more complete understanding of the coupling between the TC tilt and asymmetric boundary layer structures in sheared environments.

The structure of this paper is organized as follows: Section 2 introduces the design of the numerical simulation and various analysis methods and is then followed by an overview of the simulation in section 3. Section 4 provides an overview of the BL asymmetric structure. Section 5 examines the dynamical processes that lead to the BL asymmetries using Eulerian and Lagrangian storm-relative momentum budgets. Section 6 examines the sensitivity of the findings to different simulation choices. Results and implications are discussed in section 7. Section 8 concludes with the main findings of this study.

2. Methodology

a. Numerical model and experiment design

Cloud Model 1 (CM1; Bryan and Fritsch 2002), version 20.3, is used to perform an idealized simulation of a tropical cyclone in a moderately sheared environment. The simulated TC is on an f plane with a Coriolis parameter of $f_0 = 5 \times 10^{-5}$ s^{-1}, roughly at 20°N. The CM1 model uses an adaptively moving grid that is centered on the TC. The total size of the domain is 3996×3996 km^2 and has periodic lateral boundary conditions. The inner region has uniform 2-km horizontal grid spacing and covers 800×800 km^2. Outside this inner region, the grid spacing is stretched from 2 to 15 km. The vertical grid spacing varies from 25 m near the surface to 500 m at altitudes greater than 5500 m, with a total of 59 vertical levels.

The simulation is initialized with a modified Rankine vortex, with a maximum wind speed of 12.5 m s^{-1} at a radius of maximum wind of 75 km. In the vertical, the initial wind linearly decreases to 0 m s^{-1} at $z = 15$ km. Table 1 shows the suite of parameterization schemes used in the simulation.

Similar to previous idealized modeling studies that simulate TCs in moderate shear (Nolan 2011; Zhang and Tao 2013; Onderlinde and Nolan 2017), the CM1 model uses a large-scale nudging method (Alland et al. 2021a) to add vertical shear to the background wind field without a large-scale horizontal temperature gradient. The large-scale nudging method in CM1 nudges the domain-averaged wind field to a prescribed wind profile, rather than nudging each grid point as in the "point-downscaling method" (Nolan 2011). During the first 24 h, the simulations have no shear, after which the background wind field is gradually nudged toward a prescribed, sheared zonal background wind profile. Simultaneously, a large-scale pressure gradient force term is applied to ensure that the nudged environmental wind field satisfies geostrophic balance (Nolan 2011; Alland et al. 2021a). This prescribed wind profile has 0 m s^{-1} zonal wind for $z < 1.5$ km and has a linear westerly shear, resulting in a bulk wind difference of 7.0 m s^{-1} between $z = 1.5$ and 12 km, above which the prescribed wind is constant. The background wind reaches the prescribed profile approximately by 24 h and is then held constant thereafter.

Our goal is to examine the evolution of boundary layer asymmetries and their causes, in a precessing and intensifying TC in a moderately sheared environment. The choice of the initial vortex parameters and environmental shear profile provides an idealized, "middle-of-the-road" evolution of a cleanly precessing and intensifying TC vortex in simple, linear shear. There are a myriad of model choices that one could make to explore sensitivities, so a caveat to mention from the start is that we have not explored all the possible sensitivities to keep the investigation manageable. We will explore the sensitivity of our findings to a subset of primary model choices in section 6.

b. Horizontal wind field decomposition

In this study, we perform Helmholtz decomposition of the horizontal wind field into irrotational ($\mathbf{v}_\chi$), nondivergent ($\mathbf{v}_\psi$), and harmonic ($\mathbf{v}_{\rm env}$) components using the fast free-space Green's function method (Vico et al. 2016). This decomposition is similar to the technique introduced by Davis et al. (2008), except that Sommerfeld radiation boundary conditions are used for solving the nondivergent and irrotational winds rather than the zero Dirichlet boundary conditions. These wind components satisfy the following equations:

$$\nabla^2\psi = \zeta \quad \text{and} \quad \nabla^2\chi = \delta, \tag{1a}$$

$$\mathbf{v}_\psi = \hat{\mathbf{k}} \times \nabla\psi \quad \text{and} \quad \mathbf{v}_\chi = \nabla\chi, \tag{1b}$$

$$\mathbf{v}_{\rm env} = \mathbf{v} - \mathbf{v}_\chi - \mathbf{v}_\psi, \tag{1c}$$

where $\mathbf{v}$ is the storm-relative horizontal wind vector, $\zeta = \nabla \times \mathbf{v}$ is the relative vorticity, $\delta = \nabla \cdot \mathbf{v}$ is the horizontal divergence, ψ is the streamfunction, χ is the velocity potential, and $\hat{\mathbf{k}}$ is the vertical unit vector. As noted by Davis et al. (2008), the harmonic component $\mathbf{v}_{\rm env}$ is a good representation of the environmental wind field, especially in this case where the vorticity and divergence are dominated by the TC. Since $\mathbf{v}$ is the storm-relative wind (with the storm motion vector subtracted), $\mathbf{v}_{\rm env}$ here represents the storm-relative environmental wind. The appendix provides a detailed solving process and a comparison between $\mathbf{v}_{\rm env}$ and the environmental wind profile prescribed as part of the large-scale nudging method.

c. Measure of the TC vortex tilt

Similar to previous studies, a centroid-based method discussed in Nguyen et al. (2014) and Ryglicki and Hart (2015) is used to determine the centroid position vector of a physical field of interest σ:

$$\mathbf{x}_{\rm center} = \frac{\int_0^{2\pi}\int_0^R \sigma\,\mathbf{x}\,r dr d\lambda}{\int_0^{2\pi}\int_0^R \sigma\, r dr d\lambda}, \tag{2}$$

where $\mathbf{x}$ is the position vector, λ is the azimuthal angle, and R is the radius of integration (100 km in this study). Here, σ can be either the streamfunction ψ at a given level or column-integrated precipitating condensate $q_{\rm column} = \int \rho_d (q_{\rm rain} + q_{\rm snow} + q_{\rm graupel}) dz$, with $q_{\rm rain}$, $q_{\rm snow}$, and $q_{\rm graupel}$ being the mixing ratios of rain, snow, and graupel, respectively. As in Yu et al. (2023a,b), the centroid finding algorithm begins with the location of the minimum pressure at the level of interest and iteratively updates the centroid position using (2). Thirty iterations are used to guarantee convergence. We found that the streamfunction centroid better captures the displaced TC circulation aloft and the tilted vortex structure, resulting in a smoother vortex tilt precession evolution compared to the vorticity or pressure centroids. Therefore, in this study, the streamfunction centroid at a given level is used to define the TC center at that level. Similar to Yu et al. (2023a,b), the tilt of the TC vortex is defined as the vector difference between the TC centers at $z = 6.5$ and 1.5 km.

d. Storm-relative budgets of radial, tangential, and absolute angular momentum

Storm-relative budgets of radial and angular momentum are performed in both Eulerian and Lagrangian frameworks in this study. Following Yu et al. (2021), by taking the dot product of storm-relative momentum equations with the radial and azimuthal unit vectors (defined with respect to the translating coordinate), the storm-relative radial and tangential momentum equations are

$$\frac{Du_{\rm ST}}{Dt} = \frac{v_{\rm ST}^2}{r} + f_0 v_{\rm ST} - \frac{1}{\rho}\frac{\partial p}{\partial r} - f_0(v_g - v_c) + F_r - \frac{\partial_c u_c}{\partial t}, \tag{3}$$

$$\frac{Dv_{\rm ST}}{Dt} = -u_{\rm ST}\frac{v_{\rm ST}}{r} - f_0 u_{\rm ST} - \frac{1}{\rho}\frac{1}{r}\frac{\partial p}{\partial \lambda} + f_0(u_g - u_c) + F_\lambda - \frac{\partial_c v_c}{\partial t}, \tag{4}$$

where $u_{\rm ST}$ and $v_{\rm ST}$ are the storm-relative radial and tangential winds, ρ is total density, p is pressure, r and λ are the radius and azimuthal angle of the storm-relative coordinate, F_r and F_λ are the radial and tangential momentum sources/sinks, and

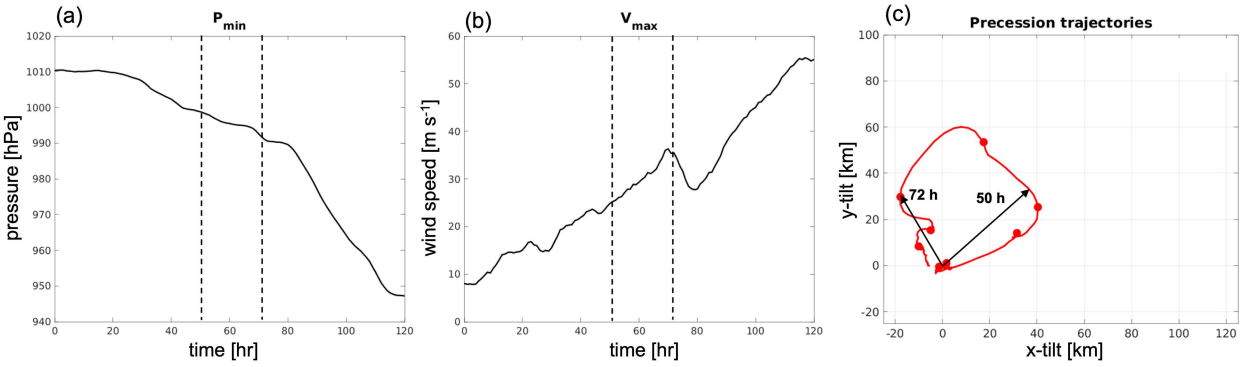

FIG. 1. Time series of the (a) minimum sea level pressure and (b) maximum 10-m wind speed of the simulated TC. Vertical dashed lines indicate $t = 50$ and 72 h, which are the beginning of the two 2-h time windows of interest. (c) The vortex centroid tilt trajectory (6.5-km centroid relative to the 1.5-km centroid at the origin) of the simulated TC. Dots are every 12 h since the start of the simulation. The two black arrows mark the vortex tilt vector at 50 and 72 h.

u_c and v_c are the radial and tangential components of the storm motion. The terms u_g and v_g are wind profiles in the x and y directions used in the large-scale nudging method. The absolute angular momentum budget can be obtained by multiplying (4) by r:

$$\frac{DM_{\mathrm{ST}}}{Dt} = -\frac{1}{\rho}\frac{\partial p}{\partial \lambda} + rf_0(u_g - u_c) + rF_\lambda - r\frac{\partial_c v_c}{\partial t}, \qquad (5)$$

where $M_{\mathrm{ST}} = rv_{\mathrm{ST}} + (1/2)f_0r^2$ is the storm-relative absolute angular momentum. Storm-relative Eulerian budgets may be obtained by expanding (3)–(5) using $D/Dt = (\partial_c/\partial t) + \mathbf{u}_{\mathrm{ST}} \cdot \nabla$, where $\partial_c/\partial t$ is the Eulerian partial time derivative in the storm-following coordinate.

3. Overview of model simulation

We first examine the intensity and vortex tilt evolution of the simulation (Fig. 1). The first 24-h spinup period has no environmental wind shear. During this 24-h spinup period, the surface pressure minimum remains steady at 1010 hPa (Fig. 1a), while the maximum surface slowly increases from 10 to about 15 m s^{-1} (Fig. 1b). After $t = 24$ h, vertical wind shear is gradually introduced using the large-scale nudging technique. Within the next 24 h ($t = 24$–48 h), the storm tilts downshear toward the east (Fig. 1c). The vortex tilt stabilizes around a magnitude of 50 km at 48 h and precesses cyclonically. The vortex tilt precesses to the upshear-left quadrant near 66 h, after which the tilt magnitude decreases as the vortex starts to realign. During the cyclonic precession period, the intensification rate is gradual, with the minimum surface pressure deepening from 1010 to 990 hPa, while the maximum surface wind increases from 15 to 30 m s^{-1} over the course of 48 h (roughly from $t = 24$ to 72 h). After 80 h,[1] the TC realigns and rapidly intensifies, with an increase in wind speed from 28 to about 58 m s^{-1} and a decrease in minimum pressure from 990 to 948 hPa during 80–120 h, although our focus here will be before this time period.

We next examine the evolution of the vortex tilt during the precession period during two different 2-h time periods: 50–52 and 72–74 h (Fig. 2). These two periods correspond to the times when the vortex tilt points toward the downshear left and upshear left (Fig. 1c), and the boundary layer exhibits asymmetric patterns representative of the overall evolution. As shown in Fig. 2a, during 50–52 h, the streamfunction at $z = 6.5$ km is shifted toward the downshear left relative to the streamfunction at 1.5 km, indicating that upper-level circulation is displaced to the downshear left. The centroid of the total precipitating hydrometeors also is displaced toward the downshear left, farther outward relative to the 6.5-km streamfunction centroid. In general, the vortex tilt direction is highly correlated with the direction of the precipitation centroid (not shown). Yu et al. (2023a) found that vorticity stretching within the rainband terminus region influences the vortex tilt magnitude and direction. Rios-Berrios et al. (2018) also found a similar alignment between the upper-level vorticity and the distribution of the saturation fraction and precipitation.

In the remainder of this study, we will focus on and nominally call the layer of air below 1.5 km as the "boundary layer." Zhang et al. (2013) defined the boundary layer height based on the inflow depth, which increases radially outward and can reach 1.5-km height. The interpretation of our results is not sensitive to how the boundary layer is precisely defined.

During 50–52 h, there are distinct asymmetries in the BL θ_E structure (Fig. 2c). Relatively low θ_E emerges in the downshear-left/downtilt direction, consistent with low-θ_E air being flushed downward in downtilt precipitation (Molinari et al. 2013; Zhang et al. 2013; Wadler et al. 2018a,b; Zhang and Rogers 2019; Li and Dai 2020; Chen et al. 2021; Alland et al. 2021a; Dai et al. 2023). Meanwhile, there is asymmetric outflow cyclonically downwind of the low-θ_E region in the upshear quadrants (hatched region).

During the later period (72–74 h) (Fig. 2b), the streamfunction fields show the vortex tilt has rotated toward the upshear-left

[1] During 72 and 80 h, a temporary fluctuation in maximum 10-m wind speed occurs as a consequence of intrusion of low-θ_E air into the TC inner core (not shown). Despite this, the minimum pressure remains undisrupted, and the TC vortex quickly resumes its circulation structure and intensifies afterward.

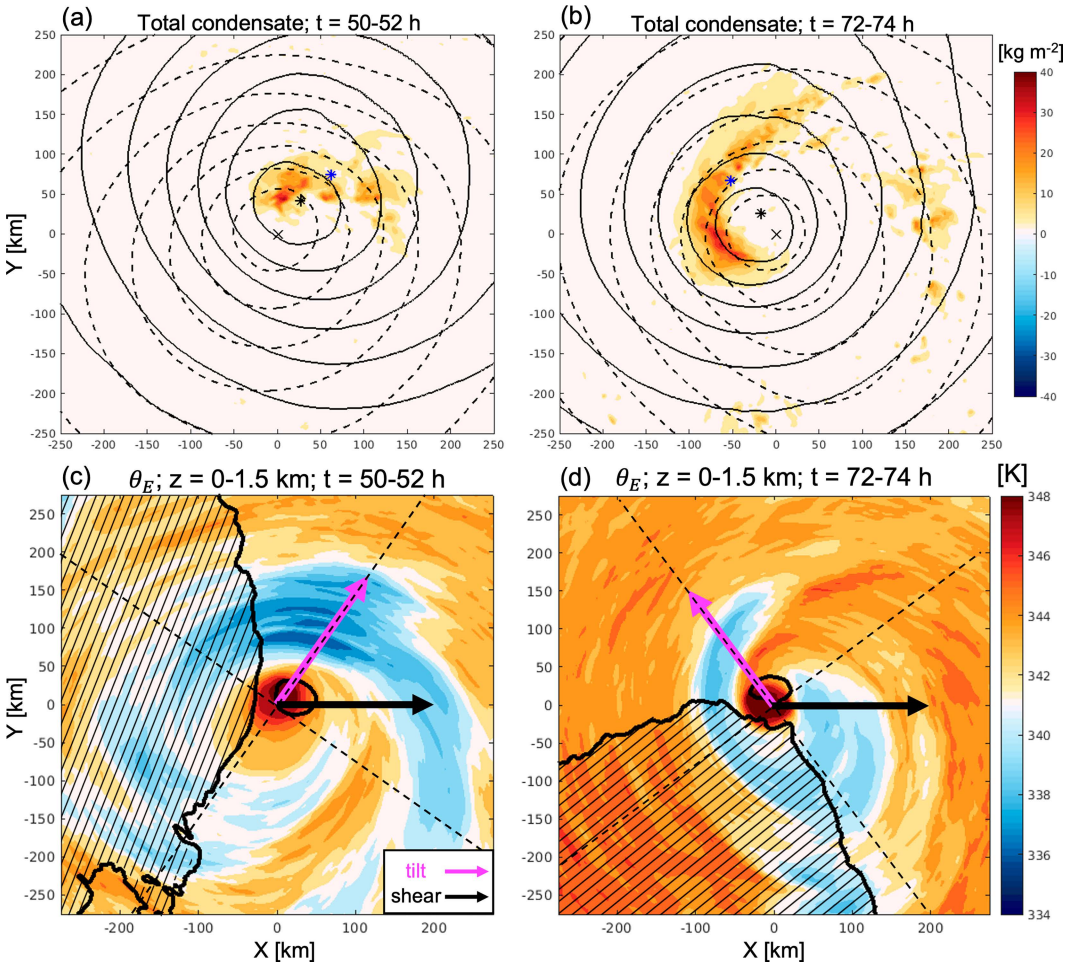

FIG. 2. Column-integrated total precipitating condensate (shaded) and centroid (blue star) for (a) t = 50–52 and (b) 72–74 h. Black dashed contours and black cross show the streamfunction and streamfunction centroid at z = 1.5 km, and solid black contours and black star show the streamfunction and streamfunction centroid at z = 6.5 km. (c),(d) The 0–1.5-km averaged θ_E for 50–52 and 72–74 h, respectively. The black hatched region shows the region with positive 0–1.5-km averaged storm-relative radial velocity (outflow). The magenta and black vectors in (c) and (d) denote the vortex tilt and shear directions, while tilt-relative quadrants are delineated by the dashed lines.

quadrant. A curved band of precipitation has become better organized and wraps upshear. Similar to the earlier period, the precipitation centroid remains aligned with the vortex tilt direction and lies outward of the 6.5-km streamfunction centroid.

The boundary layer θ_E structure (Fig. 2d) has undergone substantial changes, but still shows distinct asymmetries. The low-θ_E region now shifts upshear and uptilt, while the outflow region also shifts cyclonically to the upshear-right (USR) quadrant.

To show the evolution of the boundary layer asymmetries more clearly, we now examine the azimuth-time evolution of several variables (Fig. 3) at the outer-core region between 40- and 100-km radii. After the introduction of vertical wind shear at 24 h, outer-core low θ_E appears near 30 h and covers mainly the left-of-shear quadrants during 30–60 h. After 60 h, the lowest θ_E air extends to the upshear-right quadrant. Figure 3b shows that storm-relative radial outflow exists on the upshear side of the storm during 30–70 h, first covering the upshear-left quadrant and later extending into the upshear-right quadrant and remaining mostly there afterward. Radial inflow maximizes over the downshear-left quadrant and later extends into the upshear-left quadrant. Interestingly, the "node" of the radial flow pattern seems to closely coincide with the minimum in θ_E. On the other hand, Fig. 3c shows that the largest storm-relative tangential winds tend to be collocated with the low-θ_E air, first in the left-of-shear quadrants during 30–60 h and eventually extending into the upshear-right quadrant. The shear-relative locations of the low-θ_E air, storm-relative inflow, and strong tangential winds generally agree well with the boundary layer asymmetries shown in previous observation and modeling studies (Molinari and Vollaro 2010; Molinari et al. 2012; Zhang et al. 2013; Ming et al. 2014; Gu et al. 2015; Li and Dai 2020; Ahern et al. 2021; Alland et al. 2021a; Alland and Davis 2022; Wadler et al. 2018a,b; Wadler et al. 2022; Dai et al. 2023), but the analysis here shows some clear cyclonic propagation with time. Importantly, this

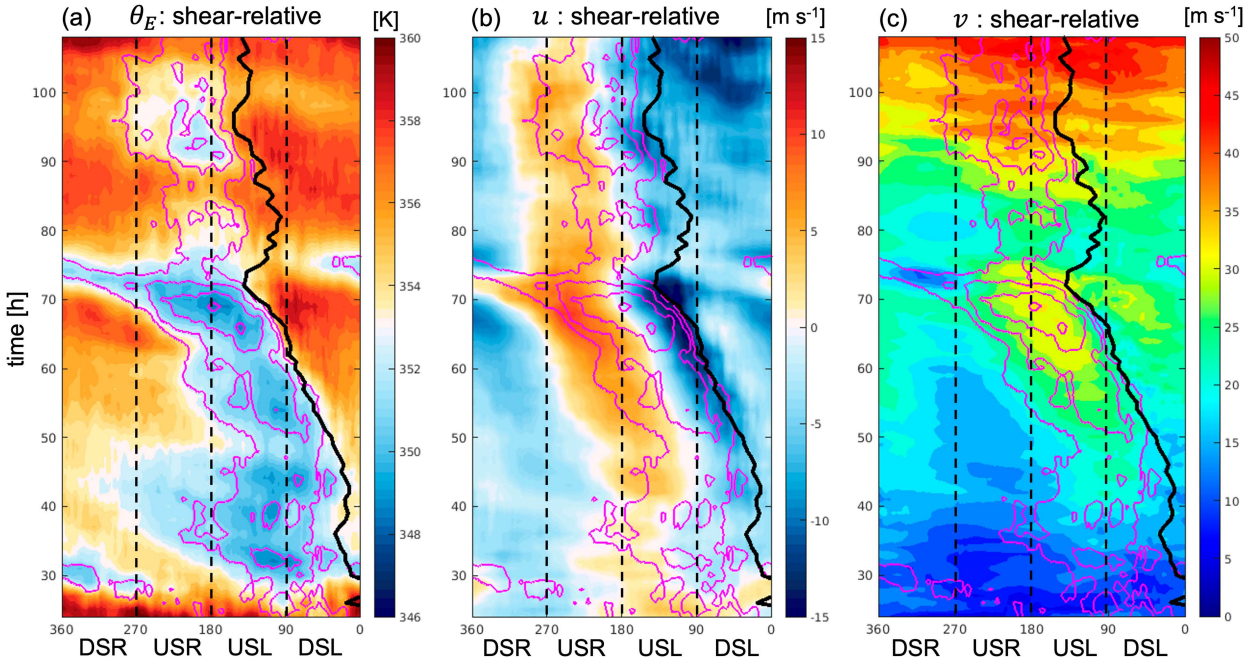

FIG. 3. (a) Shear-relative azimuthal–time plot of 0–1.5-km averaged (a) θ_E, (b) storm-relative radial wind, and (c) storm-relative tangential wind, each variable radially averaged between 40 and 100 km. The magenta contours show negative azimuthal anomalies of θ_E, every 1.6 K starting from −8 K. Shear-relative quadrants are delineated and labeled: downshear right (DSR), USR, USL, and DSL. The azimuthal angle increases cyclonically with 0° being the direction of the shear. The vortex tilt direction is shown in a thickened black line.

cyclonic propagation of the asymmetric structures in θ_E, radial velocity, and tangential velocity all follows the precession of vortex tilt closely, as shown by the black solid line in Fig. 3.

To better visualize the association between the cyclonic propagation of BL asymmetries and the vortex tilt precession, the analysis is repeated in a tilt-relative perspective, instead of a shear-relative perspective (Fig. 4). In this perspective, at leading order, the asymmetries appear quasi-stationary relative to the vortex tilt. Relatively low-θ_E air and the strongest tangential winds exist primarily left of tilt, and storm-relative outflow exists uptilt left (UTL). Thus, the asymmetric boundary layer kinematic and thermodynamic structural evolution has a strong connection with the vortex tilt. Does the phase-locked relationship between the low-θ_E, radial, and tangential wind anomalies suggest a physical coupling that explains their phase relationship to one another and the vortex tilt? We will further explore these questions in subsequent sections.

Figure 5 shows tilt-relative quadrant-averaged cross sections to compare differences in the TC structure between quadrants during t = 72–74 h when vortex tilt points toward the upshear-left direction. Other times show qualitatively similar tilt-relative quadrant differences. The strongest ascent lies downtilt (Figs. 5b,c). The downtilt-right (DTR) quadrant features broad ascent and diabatic heating between 50 and 150 km (Fig. 5c), associated with convective rainbands. The downtilt-left (DTL) quadrant has a narrower and more inward region of ascent (Fig. 5b). Radially outward and under this region of ascent are midlevel inflow, descent, and diabatic cooling. The structure is associated with a more predominant stratiform rainband structure. This descent brings low-θ_E air into the BL and is also associated with enhanced BL tangential winds (Fig. 5f). The descent and diabatic cooling extend cyclonically downwind into the uptilt-left quadrant (Fig. 5a). Within the BL, outflow exists outward of 30 km, and the BL tangential winds are anomalously weak (Fig. 5e). The uptilt-right (UTR) quadrant has relatively weak vertical motions and the weakest BL tangential winds (Figs. 5d,h). We will more closely examine how the boundary layer asymmetries noted in Figs. 3–5 connect with the vortex structure and rainband processes in the subsequent sections.

4. Kinematic overview of the boundary layer wind asymmetries

The results from section 3 show that the TC boundary layer shows clear asymmetries in both dynamic and thermodynamic variables, which propagate cyclonically with a specific azimuthal phase relationship relative to the vortex tilt. In this section, we first focus our attention on the wind anomalies to understand their kinematic properties and physical relations.

a. Tangential velocity

We first focus on the BL asymmetry of the tangential wind field. During 50–52 h, the storm-relative tangential wind at z = 900 m has a strong asymmetry, having a maximum that covers the downtilt-left quadrant (Fig. 6a). This asymmetry extends beyond the 150-km radius and overlaps with the low-θ_E region in Fig. 2c. In addition, a substantial portion of the downtilt-left tangential wind within 100-km radius is supergradient (green contour), which is an important observation

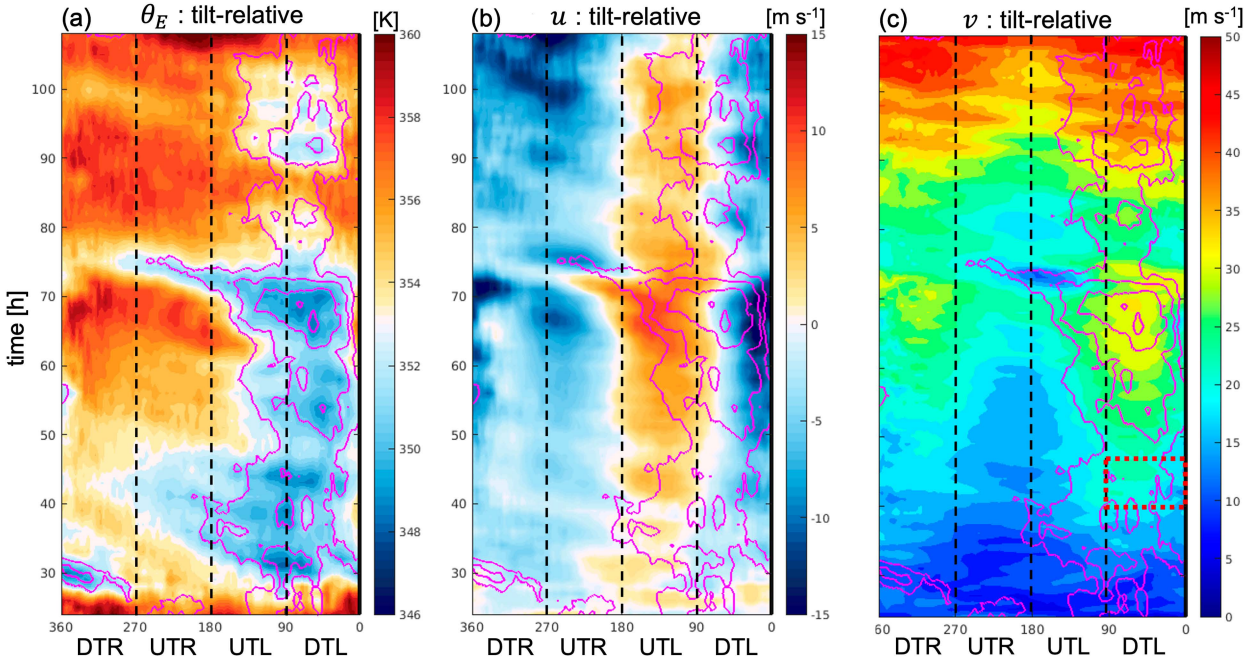

FIG. 4. As in Fig. 3, but for a tilt-relative perspective. Note that 0° now denotes the tilt direction. Tilt-relative quadrants are labeled: DTR, UTR, UTL, and DTL.

that we will return to when examining reasons for the outflow in section 5. There is also a smaller region of supergradient winds in the downtilt-right quadrant, but it is distinct from the main downtilt-left region and not the focus of our analysis. The tangential wind is predominantly nondivergent (Fig. 6b). During later hours (72–74 h) when the vortex tilt points upshear left, the orientations of the tangential wind maximum, main supergradient wind region (Fig. 6c), and nondivergent

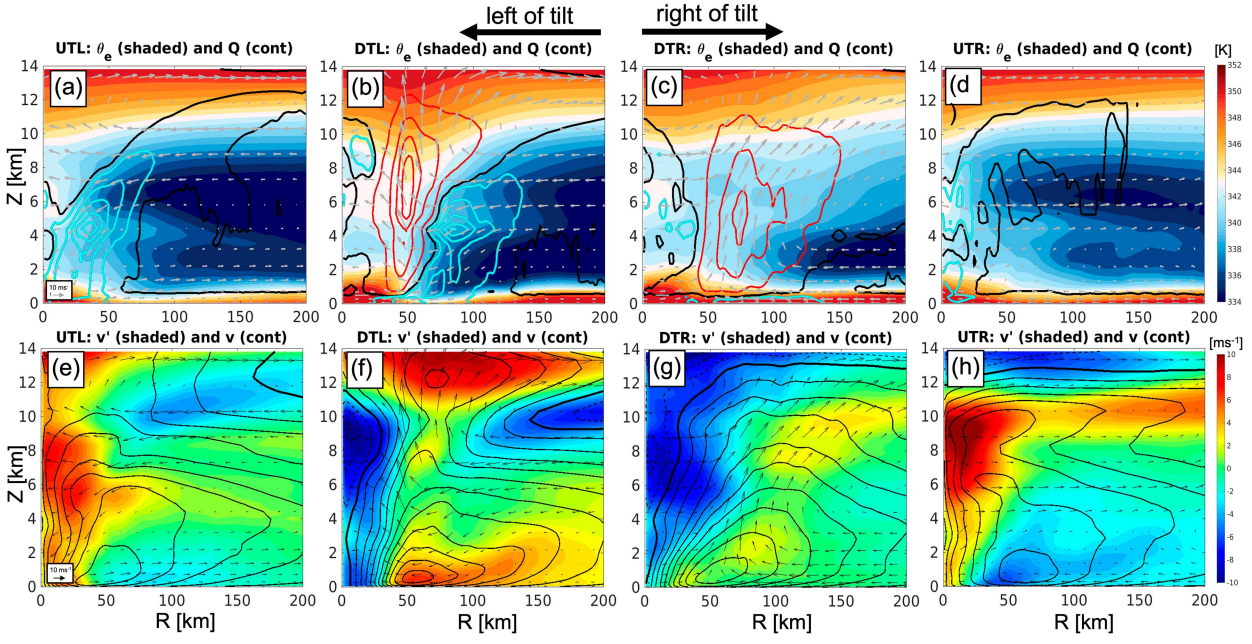

FIG. 5. Tilt-relative, quadrant-averaged sections, showing (a)–(d) θ_e (shaded) and diabatic tendencies (heating contoured in red every 0.0024 K s^{-1} from 0.0012 K s^{-1}; cooling contoured in cyan every −0.0006 K s^{-1} from −0.0003 K s^{-1}; zero contour given by the black line) and (e)–(h) tangential wind azimuthal anomaly (shaded) and full tangential wind (contoured at every 3 m s^{-1} with zero contour thickened). Vectors show the quadrant-average radial–vertical circulation.

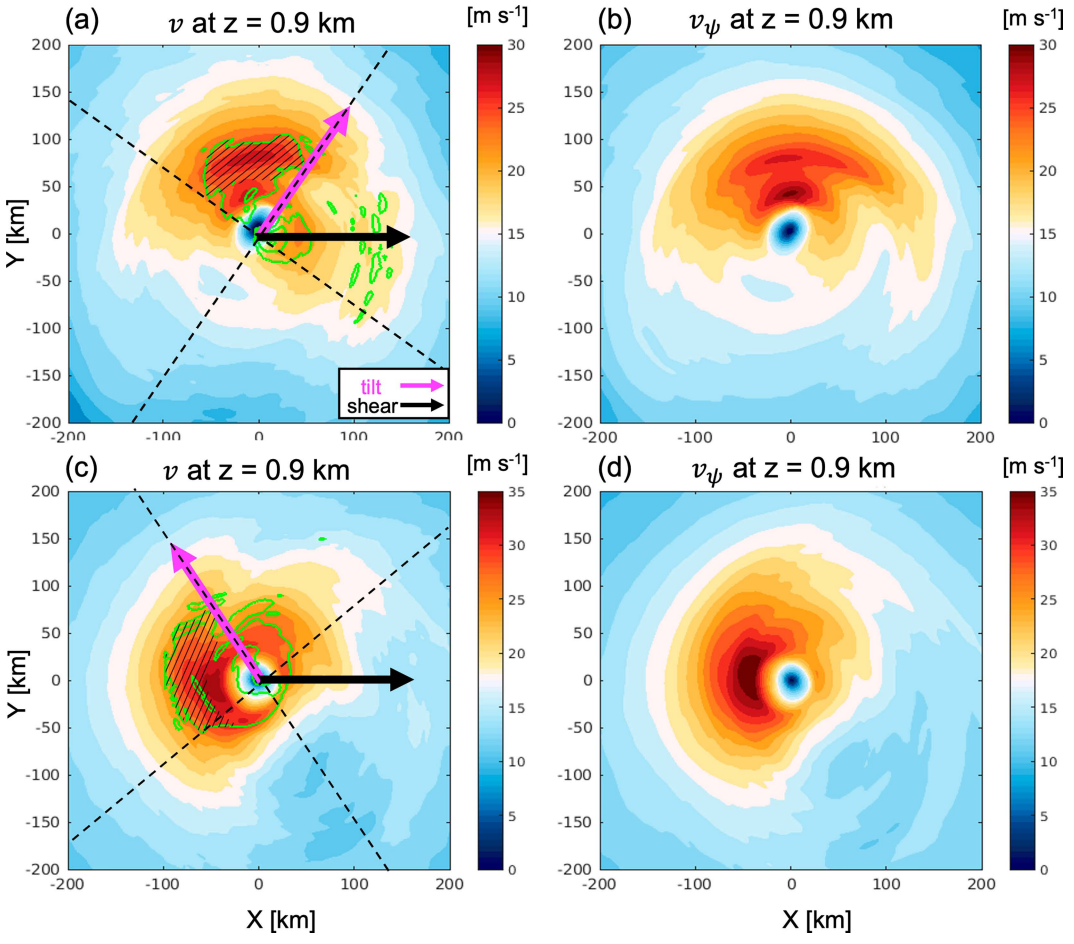

FIG. 6. The (a),(c) storm-relative tangential wind and (b),(d) its nondivergent component at $z = 0.9$ km, averaged during (top) 50–52 h and (bottom) 72–74 h. Positive gradient wind residual (supergradient) is contoured in green at 0.005 m s^{-2}. For the trajectory initialization area, the region between $r = 60$ and 100 km radius that has gradient wind residual > 0.005 m s^{-2} is hatched. The tilt direction is shown by the magenta arrows in (a) and (c), with the tilt-relative quadrants delineated. The shear direction is shown by the black arrows in (a) and (c).

wind maximum (Fig. 6d) all rotate upshear, but remain in the downtilt-left quadrant.

To relate the asymmetric tangential wind field to the distributions of relative vorticity and the nondivergent streamfunction, Fig. 7 shows that during both the 50–52- and 72–74-h periods, the streamfunction ψ contours are more closely packed in the downtilt-left quadrant, resulting in an enhanced radial gradient of ψ and thus the anomalously strong nondivergent wind (Figs. 6b,d). In addition, the downtilt-left quadrant has near-zero relative vorticity outside of the 80-km radius, indicating that the enhanced downtilt-left tangential wind is almost inertially neutral and decays as $1/r$. This is an important characteristic that we will return to when examining the downtilt-left tangential wind acceleration mechanisms in the next subsection. Meanwhile, the relative vorticity is more positive uptilt. The asymmetric distribution of vorticity causes the streamfunction to have an elliptic structure. Because of this elliptic structure of ψ, the radius along a ψ contour increases in the cyclonic direction over the uptilt-left quadrant. Since the nondivergent wind vector is always parallel to the streamfunction, the nondivergent wind has an outward radial component over the uptilt-left quadrant, as given by the red dashed arrows in Figs. 7a and 7b. The opposite happens over the downtilt-right region, where the nondivergent wind has an inflow component (green dashed arrows), contributing to an enhanced radial inflow over the downtilt-right quadrant. This shows how the asymmetric structure of relative vorticity is kinematically tied to the asymmetric nondivergent radial flow.

b. *Radial velocity*

The asymmetric structure of the BL tangential wind, supergradient wind region, and nondivergent streamfunction shown in the previous section indicates a close connection between the asymmetric radial velocity and the nondivergent circulation. To examine this connection more clearly, it is useful to decompose radial wind into nondivergent, irrotational, and harmonic (environmental) components.

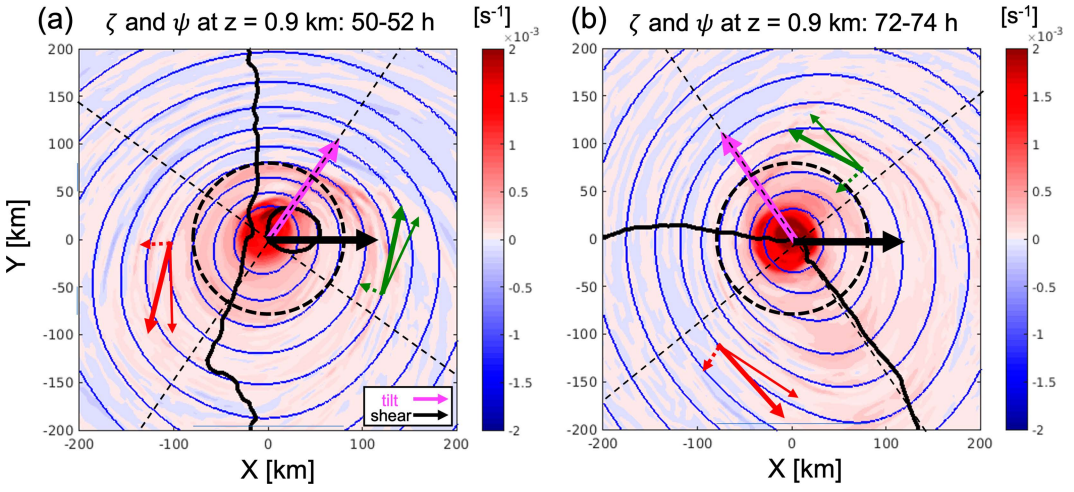

FIG. 7. Relative vorticity (shaded) and streamfunction (blue contours) at $z = 0.9$ during (a) 50–52 and (b) 72–74 h. The thick black contour shows zero nondivergent radial velocity. The tilt direction is shown in the magenta arrows, with tilt-relative quadrants delineated. The shear direction is shown by the black arrows. Red and green arrows show the decomposition of the nondivergent wind vector (thick solid arrow) into radial (dashed arrow) and tangential (thin solid arrow) components. The dashed black circle indicates a radius of 80 km.

During 50–52 h, the boundary layer radial velocity is characterized by a strong wavenumber-1 asymmetry, with radial inflow downtilt right and radial outflow uptilt left (Fig. 8a). The decomposition shows that the downtilt-right inflow has the greatest contribution from the irrotational wind (Fig. 8b), which is associated with boundary layer convergence and a rainband (not shown), with a lesser contribution from the nondivergent wind (Fig. 8c) and environmental wind (Fig. 8d). Note that the nondivergent radial wind captures a portion of the banded inflow structure in the downtilt-right quadrant. The uptilt-left outflow, on the other hand, is mainly due to the nondivergent wind and environmental wind. In particular, the nondivergent wind largely captures the spatial pattern of the outflow, while the environmental component is more uniform

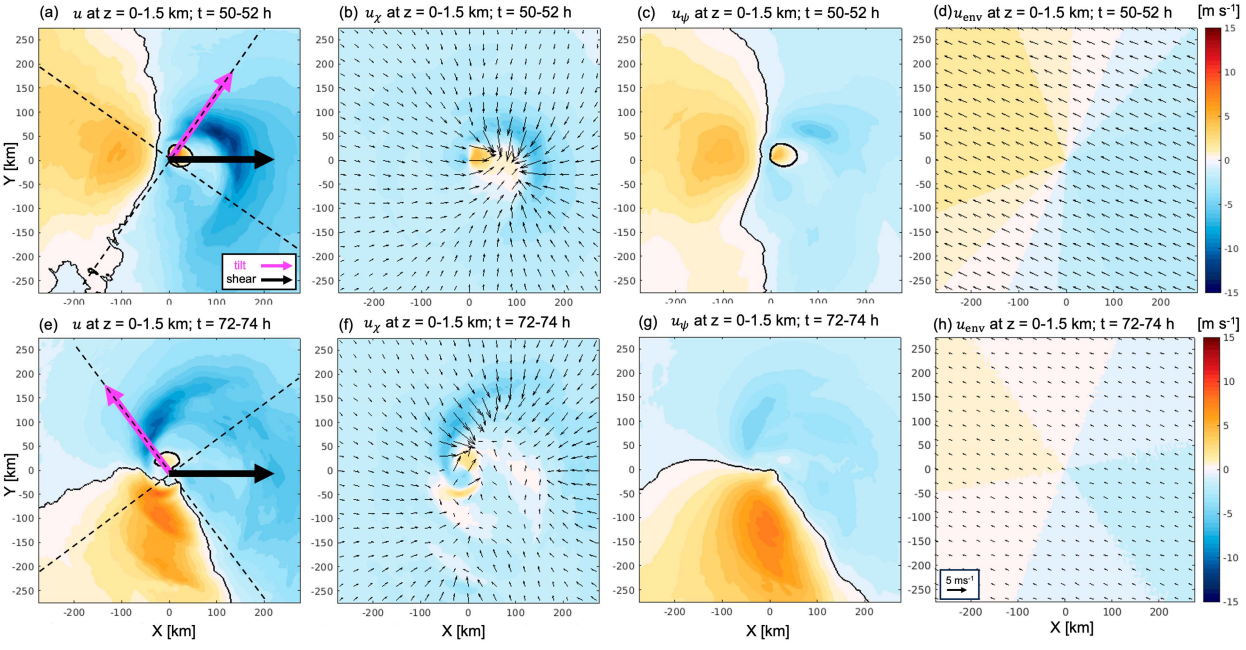

FIG. 8. The 0–1.5-km averaged radial velocity during (top) 50–52 and (bottom) 72–74 h. (a),(e) Full storm-relative radial velocity; (b),(f) irrotational component; (c),(g) nondivergent component; and (d),(h) storm-relative environmental component. The tilt direction is shown by the magenta arrows in (a) and (e), with the tilt-relative quadrants delineated. The shear direction is shown by black arrows in (a) and (e). Zero radial velocity is contoured in black in (a) and (c); irrotational and environmental wind vectors are shown in (b) and (d).

and mainly offsets the uniform inflow associated with the irrotational wind left of tilt.

When the vortex tilt points upshear left during 72–74 h (Figs. 8e–h), the wavenumber-1 pattern of the radial velocity has cyclonically shifted, with the strongest inflow lying in the upshear-left quadrant and the strongest outflow lying in the upshear-right quadrant. In the tilt-relative perspective, the location of the inflow maximum in the downtilt-right quadrant and the outflow maximum in the uptilt-left quadrant are unchanged, which is consistent with Fig. 4b. Similar to 50–52 h, the decomposition shows that the downtilt-right inflow has the greatest contribution from the irrotational wind (Fig. 8f), which is associated with convergence in the vicinity of rainband convection and some contribution from the nondivergent wind (Fig. 8g). Meanwhile, the uptilt-left outflow during 72–74 h is largely captured by the nondivergent wind, indicating that this outflow is mainly related to the vorticity distribution within the boundary layer. The environmental wind still points toward the upshear direction (Fig. 8h), differing from the overall radial outflow orientation. The results during the two time periods indicate that the main driver of the asymmetric radial outflow is largely associated with boundary layer vorticity distribution (nondivergent wind), not directly the storm-relative environmental wind or boundary layer divergence, which is consistent with the findings shown in Fig. 7.

5. Dynamic analysis of the boundary layer asymmetries

In this section, we focus on the dynamical processes that lead to the asymmetries described in section 4 to understand their origin and their relative phase relationships.

a. Storm-relative absolute angular momentum budget

We first examine the cause of the tangential wind maximum over the downtilt-left quadrant. The downtilt-left tangential wind maximum emerges near 42 h and becomes more pronounced during 42–50 h (Figs. 3c and 4c). In this section, we perform a storm-relative absolute angular momentum $[M_{ST} = rv_{ST} + (1/2)f_0r^2]$ budget over the downtilt-left quadrant to examine the processes leading to the tangential wind acceleration during this 8-h period. As discussed in section 2d, the Eulerian form of the storm-relative angular momentum budget is

$$\frac{\partial_c M_{ST}}{\partial t} = -u_{ST}\frac{\partial M_{ST}}{\partial r} - \frac{v_{ST}}{r}\frac{\partial M_{ST}}{\partial \lambda} - w\frac{\partial M_{ST}}{\partial z} - \frac{1}{\rho}\frac{\partial p}{\partial \lambda} + rF_\lambda + ru_g f_0 - u_c r f_0 - r\frac{\partial_c v_c}{\partial t}. \quad (6)$$

The first to fifth terms on the right-hand side of (6) are, respectively, the radial, tangential, and vertical advection, pressure gradient torque, and frictional torque. The last three terms on the right-hand side of (6) are forcings due to large-scale nudging, the radial flux of planetary angular momentum induced by the storm motion, and the effect due to storm motion acceleration. Figure 9a shows that during 42–50 h, M_{ST} below $z = 4$ km over the downtilt-left quadrant generally shows a broad increase from 70 to 200 km. To quantify the processes that lead to this increase in M_{ST} within this quadrant, (6) is integrated over this 8-h period using 2-min model output. The sum of all the terms on the right-hand side of (6) produces reasonable agreement with the actual change in M_{ST} during this period, as shown in Figs. 9b and 9c.

The contribution of each term on the rhs of (6) is shown in Figs. 9d–i. As shown in Fig. 9d, outside $r = 100$ km, the radial advection of M_{ST} is strongly positive within the boundary layer and between 4 and 8 km. Boundary layer inflow advects high-angular momentum air inward (Fig. 10a), providing a local source of M_{ST}. Meanwhile, the radial inflow between 4 and 8 km is even stronger than the frictional inflow within the boundary layer. This deep-layer, midlevel inflow is embedded within a stratiform precipitation region, similar to Didlake and Houze (2013), which is characterized by diabatic heating above $z = 5$ km and cooling below 5 km. Between 70- and 130-km radius, some of the midlevel inflow descends toward the boundary layer as it passes through the diabatic cooling in that region, resulting in a slantwise positive radial advection of M_{ST}.

Meanwhile, vertical advection of M_{ST} is negative over the downdraft region over $r = 70$–130 km (Fig. 9e), because M_{ST} generally decreases with height above the boundary layer (Fig. 10a). The negative vertical advection results in some cancellation with the positive radial advection, but the sum of the two terms is still positive, resulting in a net increase in M_{ST} around 70–100 km. This net positive advection indicates that the secondary circulation within the quadrant points down the M_{ST} gradient between 70 and 100 km (Fig. 10a), suggesting a wind field acceleration mechanism similar to wind field broadening caused by the rear-to-front inflow within stratiform precipitation region of the stationary rainband complex (SBC), as shown in observations (Didlake and Houze 2013; Didlake et al. 2018) and modeling studies (Yu et al. 2021, 2022), although these studies focused on mechanisms of secondary eyewall formation.

Near 30–40-km radius, the inward transport of high-angular momentum terminates as the inflow air exits the boundary layer through intense rising motion, bringing high-angular momentum into the free troposphere (Figs. 9a,b,e) and spinning up the tangential wind maximum near the eyewall region (Smith et al. 2009; Smith and Montgomery 2015). Azimuthal advection (Fig. 9g), the pressure gradient torque and large-scale nudging (Fig. 9h), and the effects of friction and motion (Fig. 9i) are shown for completeness but do not explain the tangential wind acceleration. The overall results of the angular momentum budget show that the combined effect of the inward and downward transport of larger M_{ST} is the main driver of the tangential wind acceleration below $z = 4$ km and $r = 70$–130 km, while an intense convective updraft is responsible for the spinup of tangential wind at 30–40 km in the downtilt-left quadrant.

How does the inward transport of M_{ST} by the descending inflow cause the depletion of positive vorticity over the downtilt-left quadrant outside of 80-km radius (Fig. 7)? Assuming reasonably that the absolute relative vorticity is contributed

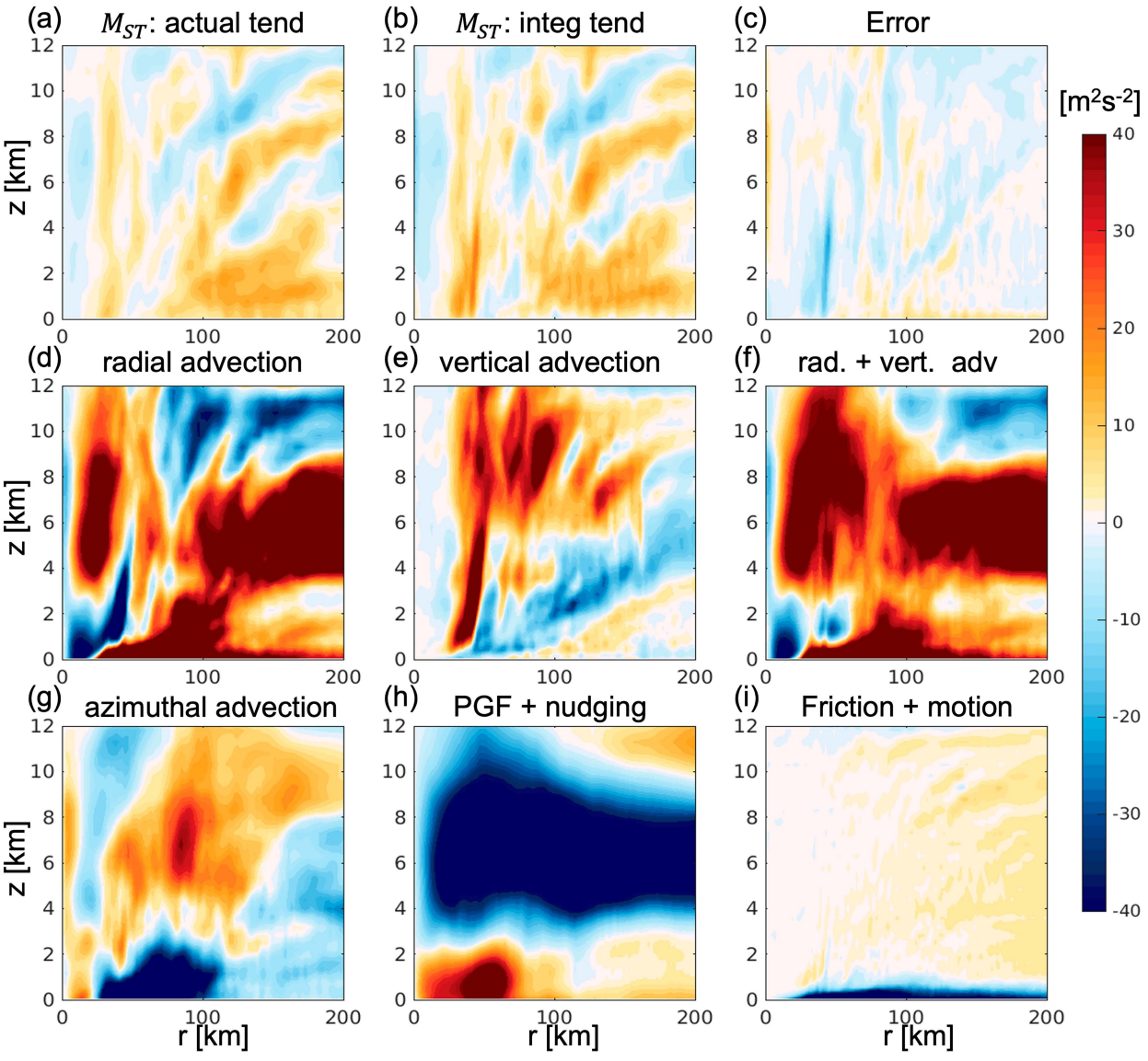

FIG. 9. DTL quadrant-averaged cross sections of absolute angular momentum budget during 42–50 h, showing (a) actual angular momentum changes, (b) integrated changes by summing terms on the rhs of (6), (c) the error (actual changes − integrated changes), (d) radial advection, (e) vertical advection, (f) sum of radial and vertical advection, (g) azimuthal advection, (h) sum of pressure gradient torque and large-scale nudging effect, and (i) subgrid-scale (turbulence and numerical diffusion) and motion-induced forcings.

mostly by the tangential wind, i.e., $\zeta_a = (1/r)(\partial r v_{ST}/\partial r) - (1/r)(\partial u_{ST}/\partial \lambda) + f_0 \approx (1/r)(\partial M_{ST}/\partial r)$, the tendency of ζ_a associated with the M_{ST} advection by the descending inflow is $(1/r)(\partial/\partial r)[-u_{ST}(\partial M_{ST}/\partial r) - w(\partial M_{ST}/\partial z)]$, i.e., proportional to the radial gradient of M_{ST} advection (Fig. 10b). As highlighted by the red dashed contour in Fig. 10a, as the descending inflow reaches the BL, the M_{ST} advection by the descending inflow maximizes near $r = 75$ km. Consequently, the radial gradient of M_{ST} advection is negative at $r > 75$ km and positive at $r < 75$ km (Fig. 10b). This dipole shows that the M_{ST} advection by the descending inflow reduces the radial gradient of M_{ST} at $r > 75$ km and increases the radial gradient of M_{ST} at $r < 75$ km, effectively redistributing the vorticity inward.[2] Therefore, the nearly zero relative vorticity (i.e., strong radial decay of tangential wind as a function of $1/r$)

[2] The redistribution property can be shown explicitly by writing the forcing term as the convergence of a general flux $\mathbf{F} = (1/r)[u_{ST}(\partial M_{ST}/\partial r) + w(\partial M_{ST}/\partial z)]\hat{r}$ (Haynes and McIntyre 1987). Focusing at z near 500 m and the red dashed contour in Fig. 10a, the radial integral of vorticity tendency from 50 to 150 km is $\int_{50km}^{150km}(1/r)(\partial/\partial r)\{r(1/r)[-u_{ST}(\partial M_{ST}/\partial r) - w(\partial M_{ST}/\partial z)]\}rdr = [-u_{ST}(\partial M_{ST}/\partial r) - w(\partial M_{ST}/\partial z)]|_{150km} - [-u_{ST}(\partial M_{ST}/\partial r) - w(\partial M_{ST}/\partial z)]|_{50km}$, which is nearly zero since both values at $z = 500$ m are close to the red dashed contour in Fig. 10a. This shows that the decrease in vorticity at the outer cooling-driven downdraft region is due to a redistribution of vorticity toward inner radii.

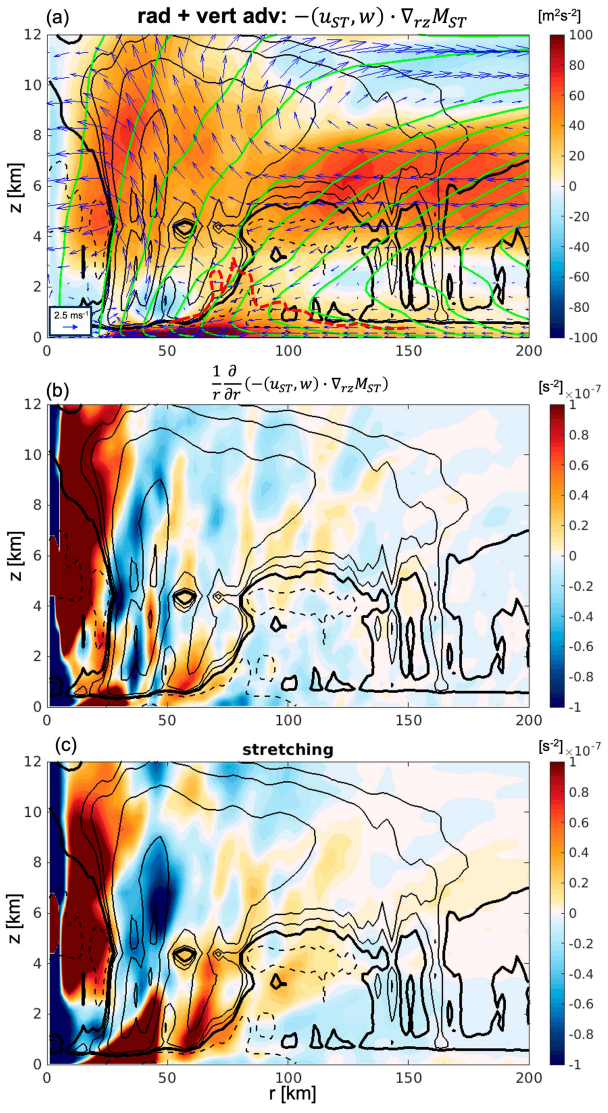

FIG. 10. DTL quadrant-averaged cross sections showing (a) the sum of radial and vertical advection of M_{ST} during 42–50 h, with the 28 m^2 s^{-2} contour between r = 50 and 150 km indicated by the red dashed line; (b) the radial gradient of the radial and vertical advection divided by r; and (c) the stretching term. Also in (a), absolute angular momentum is contoured in green every 3.125×10^5 m^2 s^{-1}, and the radial and vertical winds are plotted in blue vectors. In all panels, diabatic heating is contoured in solid black lines at [0.1, 0.2, 0.6, 1.8, 3] $\times 10^{-3}$ K s^{-1}; diabatic cooling is contoured in dashed black lines every -0.4×10^{-3} K s^{-1}; zero line is thickened.

outside of the 75-km radius is a consequence of the diabatic cooling-driven, midlevel descending inflow into the boundary layer.

Alternatively, it can be shown that $(1/r)(\partial/\partial r)[-u_{ST}(\partial M_{ST}/\partial r) - w(\partial M_{ST}/\partial z)]$ equals the sum of the advection, tilting, and stretching of ζ_a. The dominant component between 50- and 150-km radii is the vortex stretching term $-\zeta_a\delta$ (Fig. 10c), where $\delta = (1/r)[\partial(ru_{ST})/\partial r]$ is the divergence. Therefore, the dipole structure of the vorticity forcing near 75-km radius, to leading order, is caused by vorticity compression due to the diabatic cooling-driven downdraft within the precipitation region at $r > 75$ km and vortex stretching by convection at the inner edge of the surface cold pool at $r < 75$ km. However, vorticity advection and tilting do play some role, so the M_{ST} advection explanation is more complete.

In summary, the descending radial inflow within the downtilt-left rainband region is a critical feature that increases the tangential winds and redistributes the low-level vorticity within the BL. The diabatic tendency structure outside of r = 75 km has a typical stratiform structure, with heating above 5 km and cooling below 5 km. The stratiform rainband also has characteristic midlevel descending inflow that has been identified in previous studies (Didlake and Houze 2013; Didlake et al. 2018; Yu et al. 2021, 2022, 2023a).

b. *Lagrangian trajectory analysis*

To visualize the interaction between the midlevel descending inflow and the boundary layer, in this section, we perform a trajectory analysis using the Lagrangian Analysis Tool (LAGRANTO; Wernli and Davies 1997; Sprenger and Wernli 2015). We seed initial parcel locations at z = 500 m where the gradient wind residual between r = 60 and 100 km is greater than 0.005 m s^{-2} (hatched region in Figs. 6a,c) during 50–52 and 72–74 h. For each parcel, 5-h backward and 3-h forward trajectories are integrated using 2-min model output. The backward parcel trajectories show that the majority of the parcels descend from about 3–4-km altitude and are associated with low-θ_E values (Fig. 11). This trajectory analysis supports the results from the angular momentum budget that the diabatic cooling-driven, midlevel descending inflow is responsible for the inward and downward transport of higher-angular momentum air, which then results in the acceleration of the tangential winds, and area of supergradient winds, over the downtilt-left quadrant. This analysis also explains why the low-θ_E region and tangential wind maximum are collocated over the downtilt-left quadrant, as shown in Fig. 4c, because they are the results of the same airstream.

How is the boundary layer outflow farther downwind in the uptilt-left quadrant related to the upwind asymmetries in θ_E and tangential wind? To address this question, we examine the radial momentum budget, given by (3), along the same trajectories that pass through the supergradient wind region. The sum of the first three terms on the right-hand side of (3) is the gradient wind residual, the fourth term is the sum of the large-scale nudging and motion-induced Coriolis effects, the fifth term is radial momentum forcing due to friction, and the last term is the effect due to storm motion acceleration.

Figure 12a shows the results of the composite mean Lagrangian radial momentum budget for trajectories initialized over the 50–52-h period. The results for the 72–74-h trajectory initialization period are similar (not shown). Before −50 min (trajectory time), the negative gradient wind residual results in the inward acceleration of the air parcels (Fig. 12a), gradually strengthening the negative radial velocity (Fig. 12b). From −50 to 90 min, parcels experience a strong, positive gradient wind residual and positive radial acceleration. As a result, the

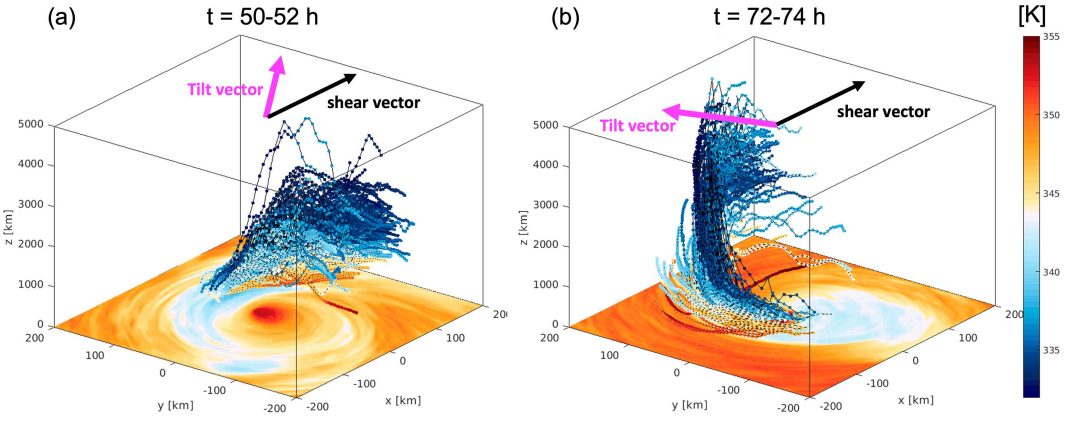

FIG. 11. Three-dimensional view of 3-h backward trajectories for an initialization period of (a) 50–52 and (b) 72–74 h. The trajectories are initialized at $z = 500$ m over the DTL quadrant where the gradient wind residual is greater than 0.005 m s^{-2} (hatched region in Figs. 8a,c; see text for details). The trajectories are colored by the θ_E along the trajectories. 0–1-km averaged θ_E during the two respective periods is shaded at the bottom of the box. Shear and tilt directions are given by the black and magenta arrows, respectively.

negative radial velocity decelerates (becomes less negative) during this period and becomes radial outflow at +25 min. Given these parcels are relatively cold (have a low θ_E), as a result of the aforementioned diabatic cooling, they are mostly confined to the BL. This sequence of events explains why the boundary layer outflow tends to occur in the uptilt-left quadrant, which is cyclonically downwind from the negative anomaly of θ_E and supergradient tangential wind maximum in the downtilt-left quadrant.

This uptilt-left outflow also contributes to the anomalous area of positive vorticity uptilt, causing the elliptic structure of the BL vorticity and streamfunction field (Fig. 7). A vorticity budget over the uptilt quadrant (not shown) shows that the uptilt quadrant has a positive vorticity tendency between 50- and 100-km radii, which is caused by a horizontal convergence of vorticity flux. The convergence of the flux is dominated by advection by the nondivergent wind. This suggests that the uptilt-left BL outflow is responsible for transporting the inner-core large relative vorticity outward and cyclonically downwind, resulting in enhanced vorticity uptilt and the elliptic vorticity structure.

The outward acceleration of parcels in the downtilt-left supergradient wind region and the resulting outflow at the uptilt-left quadrant could be relevant to the boundary layer recovery mechanism suggested by Zhang et al. (2013). As shown in Fig. 13, the forward trajectory density distribution shows that even though the downtilt-left air parcels have low θ_E initially, the parcels accelerate outward as the flow becomes supergradient. This outward acceleration prevents these low-θ_E parcels from directly intruding into the high-θ_E inner core. Rather, combined with the greater air–sea thermodynamic disequilibrium these parcels initially have and their pathlength around the storm, there is more opportunity for the recovery of their θ_E through surface heat fluxes (Fig. 13). As these parcels circulate around the TC and recover their enthalpy, they feed into the downtilt-right quadrant and

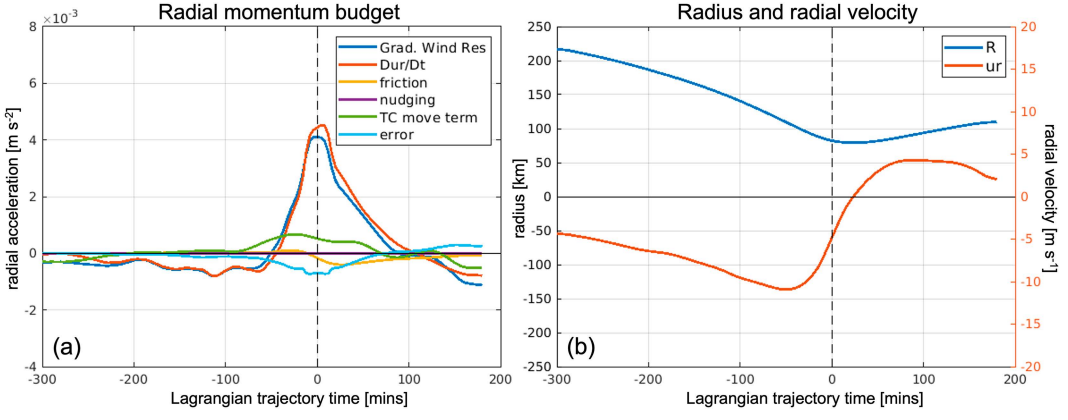

FIG. 12. Trajectory-averaged time series of the (a) Lagrangian budget of storm-relative radial momentum and (b) radius and radial velocity for trajectories initialized over the 50–52-h time period. The time axis is relative to the trajectory initialization time.

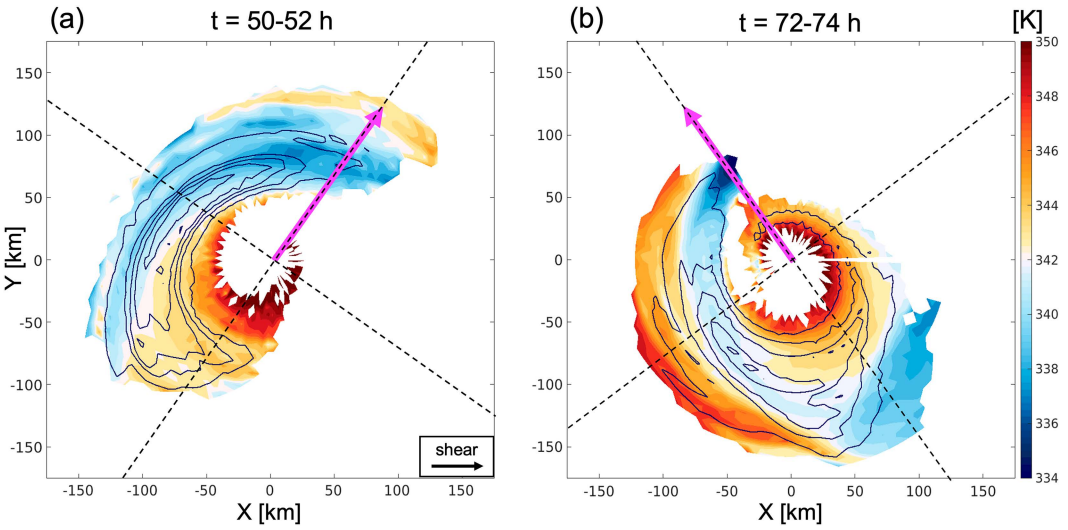

FIG. 13. Trajectory density distribution (contoured) and mean θ_E (shaded) of 3-h forward Lagrangian trajectories, initialized at (a) 50–52 and (b) 72–74 h (within hatched regions of Figs. 6a,c). The trajectory density is normalized by the peak value and is contoured every 0.2, starting from 0.1. Magenta arrows show the vortex tilt direction.

modulate the downtilt convective organization in the TC inner core and rainband region.

6. Sensitivity to parameterizations and storm motion

One important question is whether the above results are sensitive to simulation choices. There are a multitude of sensitivity tests one could run, such as altering the shear structure/magnitude and other aspects of the initialization and model configuration, so we present only a subset of possibilities to demonstrate the robustness of our findings. Table 2 shows the sensitivity experiments that we conducted, varying the choice of the boundary layer and microphysics schemes. We also performed one experiment with an initially shallower vortex, one experiment with stronger shear (15 m s^{-1}), and four experiments adding different environmental mean wind directions to impart storm motion. In addition to the Louis scheme, we tested two other boundary layer schemes: the YSU scheme and the MYNN scheme. For microphysics, we repeated the simulation with the Thompson scheme. To test the sensitivity to environmental mean wind direction, four different directions of mean wind (easterly, westerly, northerly, and southerly) were tested, all of which have a magnitude of 3.5 m s^{-1}. Among all these experiments, except the experiment with stronger shear, the environmental shear remains the same—a westerly unidirectional shear of 7 m s^{-1} between z = 1.5 and 12 km. All other model settings are identical to the simulation analyzed in previous sections (referred to as CTRL), except that a minimum horizontal grid spacing of 4 km is used for computational efficiency. This coarser grid spacing does not change the fundamental results.

As shown in Figs. 14a–d, employing different microphysics, boundary layer schemes, and vortex initial depth does not change the main result—the asymmetries in the radial wind and location of negative θ_E anomalies maintain the same quasi-stationary configuration relative to the vortex tilt and azimuthal phase relationship between variables, similar to CTRL (Fig. 4b). The overlap of the negative θ_E anomalies with the supergradient wind region (not shown) suggests the midlevel descending inflow is likewise responsible and the same mechanisms are present in these sensitivity experiments. Different schemes do affect the strength and temporal variations

TABLE 2. List of sensitivity experiments.

Experiment	Microphysics, PBL, and mean wind (u, v; m s^{-1})	Figure No.
CTRL	Morrison double moment, Louis (0, 0)	Fig. 4b
YSU	Morrison double moment, YSU (0, 0)	Fig. 14a
MYNN	Morrison double moment, MYNN-level 2.5 (0, 0)	Fig. 14b
Thompson	Thompson, Louis (0, 0)	Fig. 14c
Shallow vortex	Initial vortex depth halved to 7.5 km	Fig. 14d
Strong shear	15 m s^{-1} shear	Fig. 14e
Easterly	Morrison double moment, Louis (−3.5, 0)	Fig. 15a
Westerly	Morrison double moment, Louis (3.5, 0)	Fig. 15b
Northerly	Morrison double moment, Louis (0, −3.5)	Fig. 15c
Southerly	Morrison double moment, Louis (0, 3.5)	Fig. 15d

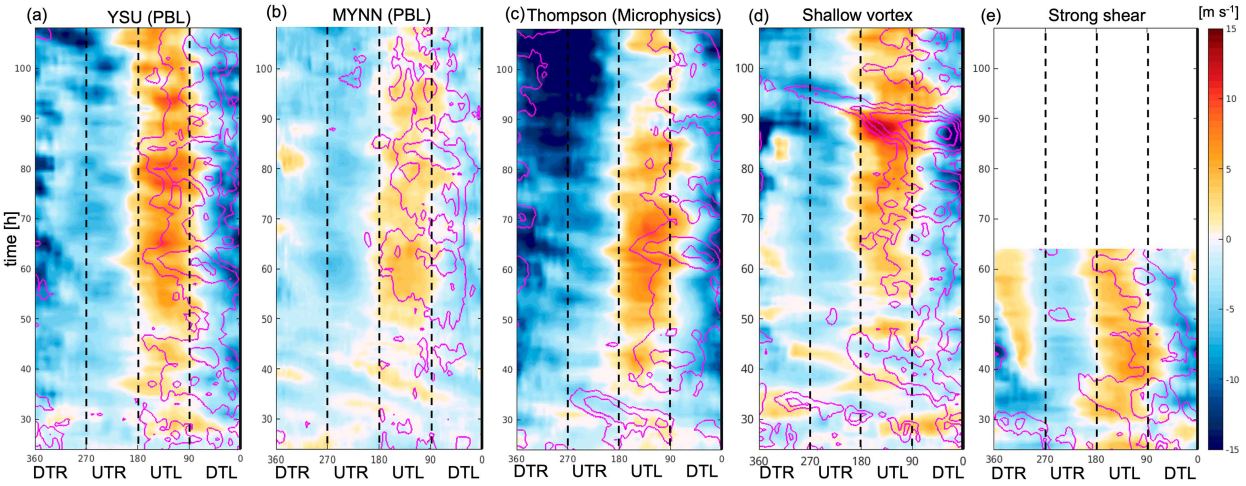

FIG. 14. Tilt-relative azimuthal-time plot of the (a)–(c) parameterization sensitivity experiments, (d) shallow vortex with initial vortex top set to 7.5 km (half of CTRL), and (e) strong shear experiment, showing the 0–1.5-km vertically averaged radial velocity, radially averaged between 40 and 100 km. Magenta lines show negative anomalies of θ_E every 1.6 K, starting from −8 K. Tilt-relative quadrants are delineated and labeled. See Table 2 for a description of the sensitivity experiments.

of anomalies. For example, the MYNN experiment has weaker anomalies overall.

In the strong shear experiment (Fig. 14e), the same relationship exists between the tilt and BL asymmetries, except that the TC vortex is sheared apart near 64 h and weakened afterward. Due to the strong shear, the vortex tilt remains downshear without showing a clear cyclonic precession (not shown), and the BL asymmetries remain roughly quasi-stationary relative to both the vortex tilt and shear. Similar quasi-stationary asymmetries relative to the shear direction in a strong shear environment are also shown in Li and Dai (2020) and Dai et al. (2023).

The main results as CTRL also hold true when testing the sensitivity to the presence and direction of the environmental mean wind (Fig. 15), which affects the storm motion. The asymmetries are predominately tilt, not motion, driven in a moderately sheared environment. These results confirm the robustness of the results discussed previously. We reiterate the caveat that we have not explored all the possible sensitivities, so it is possible there are specific choices of initial conditions or other model choices that may result in a deviation from these findings.

7. Discussion

The quasi-stationary structure of the asymmetries relative to the vortex tilt has a couple of implications. First, while many previous studies analyzed BL asymmetries in a shear-relative perspective and showed an association between shear direction and BL asymmetries, our results herein indicate that the primary driver of the evolution of the BL asymmetries is

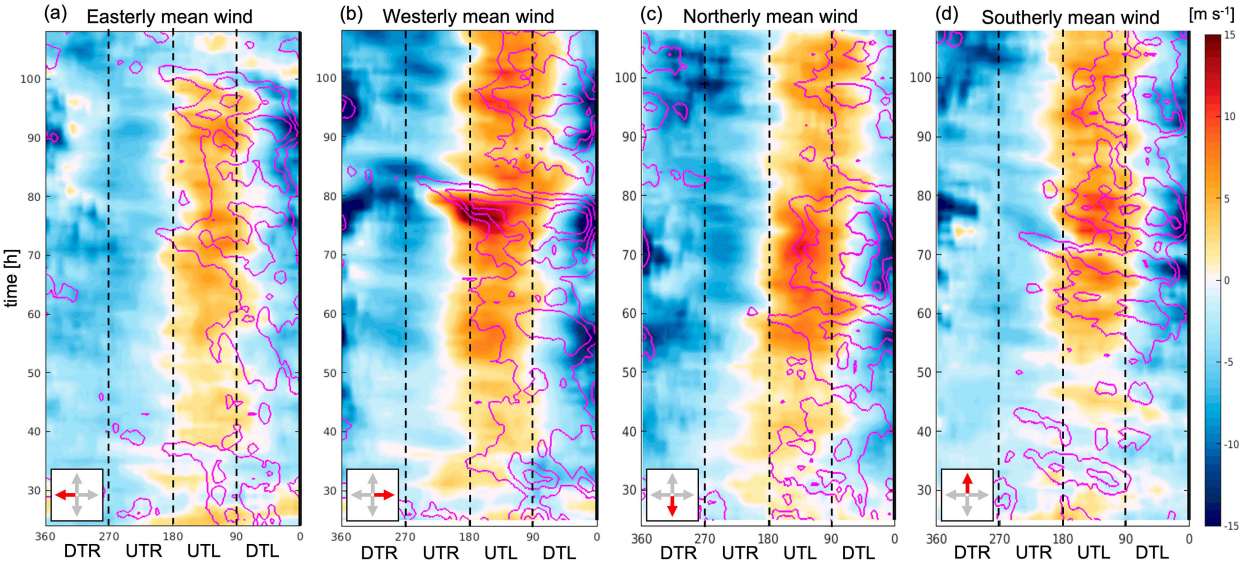

FIG. 15. As in Fig. 14, but for sensitivity experiments with different environmental mean wind directions.

the vortex tilt, not the shear itself. The important roles of vortex tilt in modulating convection distribution are well documented, including the role of balanced vortex dynamics (Raymond 1992; Jones 1995; Gu et al. 2018; Boehm and Bell 2021) and enhanced BL frictional convergence downtilt (Reasor et al. 2013; Riemer 2016; Schecter 2022). Processes controlling the vortex tilt, rainband convection, and boundary layer structure are all two-way interactions, which causes these features to couple and coevolve during the vortex precession. As a result, when viewed in a tilt-relative perspective, the BL asymmetries appear to be quasi-stationary.

Despite our emphasis on the role of the vortex tilt, the vertical wind shear plays an important role in tilting the vortex in the first place, so the shear is still a critical ingredient in producing asymmetries. Given that the vortex tilt spends most of the time in the downshear-left quadrant (Reasor et al. 2000, 2013; Schecter 2015; Tao and Zhang 2014; Rios-Berrios et al. 2018; Schecter and Menelaou 2020; Fischer et al. 2022; Yu et al. 2023a,b), it is not surprising that an association between shear direction and boundary layer asymmetries has been identified. Our findings here clarify the role of shear versus tilt.

The second implication is that the orientation of asymmetries may give indirect information about the concurrent direction of the vortex tilt relative to the shear. For instance, if the boundary layer low-θ_E region is located over the left-of-shear side and storm-relative outflow is located in the upshear-left quadrant, it would suggest the vortex tilt is pointing toward the downshear or downshear-left quadrant, a stable tilt configuration that could lead to a delay of TC intensification. On the other hand, if the low-θ_E region is located over the upshear side and storm-relative outflow is located in the upshear-right quadrant, it would suggest that the vortex tilt has precessed to the upshear-left quadrant, indicating that symmetrization of convection and vortex realignment could be underway, and intensification could be imminent (Rogers et al. 2013; Hazelton et al. 2015; Wadler et al. 2018a). This suggests that enhancing data coverage with dropsonde, radar, and other observations to diagnose the BL θ_E structure and storm-relative flow can help us better understand the concurrent vortex structure and the variability of TC intensity change in moderate vertical shear (Rios-Berrios and Torn 2017). In addition, the close linkage between vortex tilt and BL asymmetries also suggests that the evolution of BL asymmetries may be understood by diagnosing the vortex tilt evolution, which could be approximated using the horizontal vorticity budget in a rotating coordinate (Yu et al. 2023a).

8. Conclusions

In this study, we examined the sequence of events that leads to the asymmetric boundary layer structure of a tropical cyclone in a moderately sheared environment. The foci were to understand the driving mechanism of the asymmetric boundary layer structure that has been identified in previous studies, the physical reasons for the azimuthal phase relationship between asymmetries of certain variables, and the connection of vortex tilt to these asymmetries.

In a shear-relative perspective, the boundary layer radial and tangential velocities, along with θ_E, show an asymmetric structure that is consistent with previous observational studies. When the TC is tilted toward the downshear left, negative θ_E anomalies exist left of shear and are collocated with positive tangential wind anomalies. The radial wind, on the other hand, has enhanced inflow downshear and outflow upshear. Importantly, these asymmetries all exhibit clear cyclonic propagation over time, which is closely coupled with the cyclonic precession of the vortex tilt in the simulation.

In a tilt-relative perspective, in contrast, these boundary layer asymmetries are quasi-stationary relative to the vortex tilt and the asymmetries have an azimuthal phase relationship between one another. At the downtilt-left quadrant, negative θ_E anomalies collocate with positive tangential wind anomalies, which are supergradient. The largest inflow occurs downtilt, and radial outflow occurs in the uptilt-left quadrant. The uptilt-left outflow is mainly associated with the nondivergent flow of the elliptical vorticity structure and cannot be fully explained by the storm-relative environmental flow alone.

Figure 16 illustrates the important rainband processes that couple these asymmetries with the vortex tilt. As the tilt-induced rainband convection transitions into stratiform precipitation in the downtilt-left quadrant, horizontal buoyancy gradients within the precipitation region drive midlevel descending inflow (MDI), which brings both midlevel low-θ_E and high-angular momentum air into the BL. A quadrant-averaged angular momentum budget shows that this descending inflow causes asymmetric tangential wind acceleration within the downtilt-left quadrant, resulting in broadscale supergradient flow in the BL. The outward-directed agradient force decelerates the inflow, preventing the direct intrusion of low θ_E into the inner core and resulting in outflow cyclonically downwind at the uptilt-right quadrant. As the BL low-θ_E air circulates around the TC center in an elliptical trajectory, it recovers its θ_E through surface enthalpy fluxes (Molinari et al. 2013; Zhang et al. 2013; Wadler et al. 2018a,b; Nguyen et al. 2019; Zhang and Rogers 2019). Given the MDI transports both low-θ_E air and high-angular momentum air down into the boundary layer, the tangential wind maximum and low-θ_E region tend to collocate in the downtilt-left quadrant. The sequence of events described herein explains the observed BL asymmetries, including the collocation of negative θ_E anomalies and enhanced tangential wind in the downtilt-left quadrant, the largest inflow downtilt, and the radial outflow in the uptilt-left quadrant.

In terms of the BL vorticity and circulation structure, the advection of angular momentum by the MDI, maximized at the inner edge of the boundary layer low-θ_E region, acts to dilute the relative vorticity in the diabatic cooling-driven downdraft region (via vortex compression) and concentrate the relative vorticity in the inner convective updraft region (via vortex stretching). Meanwhile, outflow in the uptilt-right quadrant contributes to horizontal vorticity flux convergence in the uptilt-half semicircle. These two processes together result in an elliptic structure in the BL vorticity and streamfunction.

We examined whether the findings were sensitive to storm motion, stronger shear, vortex depth, and different boundary

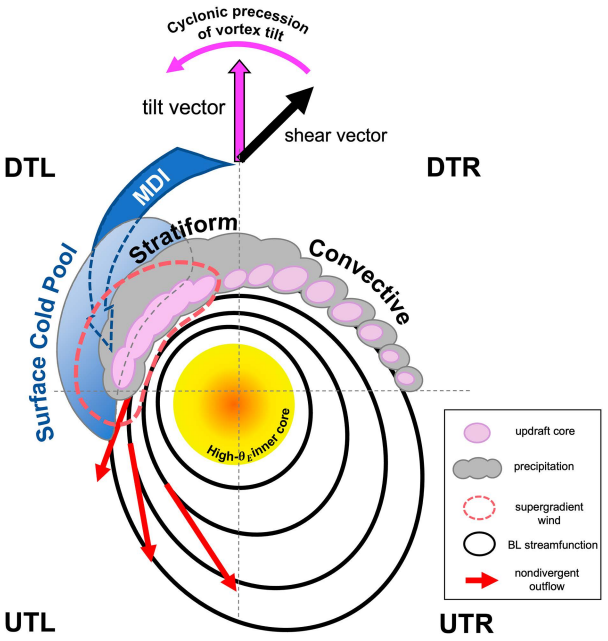

FIG. 16. Schematic diagram showing the organization of TC rainband convection and precipitation, MDI, BL asymmetric cold pool (low-θ_E air), and BL streamfunction for a tilted TC vortex in shear. The red dashed contoured region shows the main region of the supergradient tangential winds, where the streamfunction (black contours) gradient is larger. Red arrows indicate nondivergent wind vectors over the UTL quadrant that have an outflow component.

layer and microphysics parameterizations. Sensitivity experiments varying these choices indicate that the quasi-stationary nature of the asymmetries relative to the tilt direction remains consistent. Therefore, in sheared environments, tilt (vs shear or motion direction) appears to be a more relevant factor organizing BL asymmetries. This finding is consistent with previous studies that used more complex sheared profiles (Onderlinde and Nolan 2016). Using similar shear profiles as in Onderlinde and Nolan (2016) and Gu et al. (2018) showed that the BL inflow and asymmetric upward motions of a dry, tilted vortex are tightly phase locked with vortex tilt, regardless of whether the sheared flow is veering or backing with height. Their results similarly indicate that vortex tilt is the dominant factor determining the vortex-scale asymmetries, not the deep-layer shear. Therefore, we speculate that our finding regarding the relationship between vortex tilt and BL asymmetries would hold in more complex shear environments.

The BL asymmetric structures were simulated in an idealized environment where the environmental shear is predefined and can be fully separated from the TC vortex. Further analysis is needed to examine whether the same relationships between asymmetries and tilt can be reproduced in more complex environments, such as when including the β effect. While we have examined the sensitivity of our findings to different mean wind directions, the storm translation speed in all the sensitivity experiments is about 2.5–5.5 m s^{-1}. Results could differ under stronger mean winds with faster translation speeds, which can induce strong asymmetries in surface fluxes and further impact boundary layer θ_E asymmetries. This effect may be tested to further generalize these results. Additionally, more unusual alignment and intensification pathways, such as downshear reformation, were not examined due to our desire to have a relatively straightforward, canonical experiment to analyze. Real-case simulations would be interesting to examine as follow-on work to evaluate the hypotheses herein. For example, Ahern et al. (2021) identified similar features in a simulation of Hurricane Irma (2017), involving the descending inflow, BL low-θ_E region, and outflow. Whether or not the same tilt-relative asymmetries and associated mechanisms apply across a range of TC stages would be of additional interest.

Acknowledgments. We thank Dr. Kyle Ahern for his thoughtful discussion on this study. Three anonymous reviewers provided valuable feedback to improve this study. This research was supported by the Office of Naval Research Grants N000142012071 and N000142312443.

Data availability statement. The CM1 namelist files and model output are available upon request via a University at Albany Thematic Real-time Environmental Distributed Data Services (THREDDS) server.

APPENDIX

Helmholtz Decomposition of the Horizontal Wind Field

In this appendix, we document the Helmholtz decomposition procedure of the horizontal wind field and provide an assessment of the agreement between the diagnosed environmental wind field and the imposed environmental wind profile in the large-scale nudging of the CM1 model.

The solutions for ψ and χ of (1a) are solved using the Green's function approach (Schot 1992; Vico et al. 2016). In general, the solution of the Laplacian equation ($\nabla^2\phi = f_\phi$) that satisfies the Sommerfeld radiation boundary condition is

$$\phi(\mathbf{x}) = \left(\frac{1}{2\pi}\right)^2 \int_{R^2} e^{i\mathbf{s}\cdot\mathbf{x}} \frac{F_\phi(\mathbf{s})}{|\mathbf{s}|^2} d\mathbf{s}, \tag{A1}$$

where is $\mathbf{s}$ is the frequency vector in the Fourier domain and $F_\phi(\mathbf{s}) = \int_D e^{-i\mathbf{s}\cdot\mathbf{x}} f_\phi(\mathbf{x}) d\mathbf{x}$ is the Fourier transform of the source function $f_\phi(\mathbf{x})$ over its domain D. The Sommerfeld radiation boundary condition yields a unique solution that radiates from its source function (Schot 1992; Vico et al. 2016), as if it is residing in an infinitely large domain. This property minimizes artifacts at the boundaries that arise due to the limited domain size of the solving grid. An additional benefit of the uniqueness of the solutions for ψ and χ is that it admits a unique harmonic component $\mathbf{v}_{\text{env}}$ for a given $\mathbf{v}$ vector field using (1c). Equation (1a) is solved for ψ and χ using the vorticity ζ and divergence δ from the entire 4000 × 4000 km^2 model domain with the fast convolution method introduced in Vico et al. (2016).

In the decomposition, the motion-induced wind field is embedded into the harmonic components $\mathbf{v}_{\text{env}}$, meaning that if $\mathbf{v}$

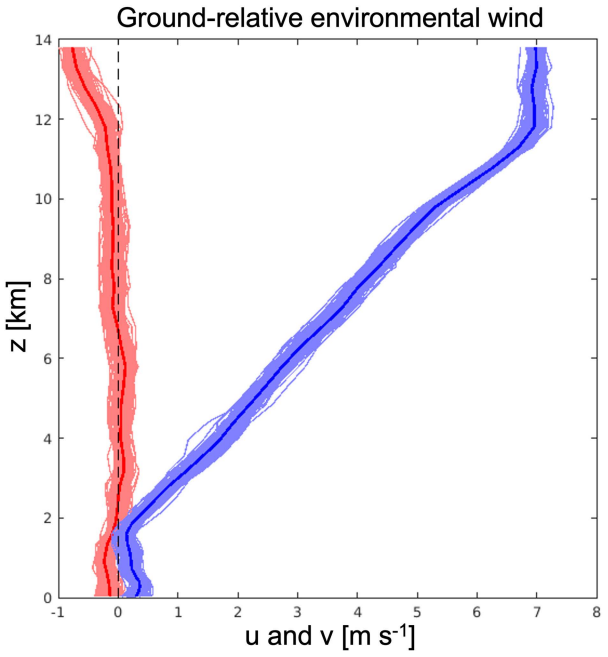

FIG. A1. Profiles of ground-relative environmental zonal wind (blue) and meridional wind (red) at every three grid points within the 800 × 800 km^2 fine-grid domain during 50–52 h. The thicker blue and red lines are the domain-averaged wind profiles.

is the storm-relative wind vector, then $\mathbf{v}_{env}$ is the storm-relative environmental wind. The ground-relative environmental wind can be recovered by adding the storm motion to $\mathbf{v}_{env}$. To verify the correctness of the wind field decomposition, we examine the diagnosed ground-relative environmental wind to assess whether it is consistent with the prescribed wind profile used in the large-scale nudging. As shown in Fig. A1, the ground-relative u and v environmental wind profiles at each grid point are quite uniform and agree nicely with the prescribed wind profiles (as described in section 2a) during 50–52 h. The results for 72–74 h are similar (not shown). This result verifies the accuracy of the wind field decomposition and that the simulated storm is embedded in a uniformly sheared environment.

REFERENCES

Ahern, K., R. E. Hart, and M. A. Bourassa, 2021: Asymmetric hurricane boundary layer structure during storm decay. Part I: Formation of descending inflow. *Mon. Wea. Rev.*, **149**, 3851–3874, https://doi.org/10.1175/MWR-D-21-0030.1.

Alland, J. J., and C. A. Davis, 2022: Effects of surface fluxes on ventilation pathways and the intensification of Hurricane Michael (2018). *J. Atmos. Sci.*, **79**, 1211–1229, https://doi.org/10.1175/JAS-D-21-0166.1.

——, B. H. Tang, K. L. Corbosiero, and G. H. Bryan, 2021a: Combined effects of midlevel dry air and vertical wind shear on tropical cyclone development. Part I: Downdraft ventilation. *J. Atmos. Sci.*, **78**, 763–782, https://doi.org/10.1175/JAS-D-20-0054.1.

——, ——, ——, and ——, 2021b: Combined effects of midlevel dry air and vertical wind shear on tropical cyclone development. Part II: Radial ventilation. *J. Atmos. Sci.*, **78**, 783–796, https://doi.org/10.1175/JAS-D-20-0055.1.

Barnes, G. M., and K. P. Dolling, 2013: The inflow to tropical Cyclone Humberto (2001) as viewed with azimuth – Height surfaces over three days. *Mon. Wea. Rev.*, **141**, 1324–1336, https://doi.org/10.1175/MWR-D-11-00348.1.

Bhalachandran, S., Z. S. Haddad, S. M. Hristova-Veleva, and F. D. Marks Jr., 2019: The relative importance of factors influencing tropical cyclone rapid intensity changes. *Geophys. Res. Lett.*, **46**, 2282–2292, https://doi.org/10.1029/2018GL079997.

Black, M. L., J. F. Gamache, F. D. Marks Jr., C. E. Samsury, and H. E. Willoughby, 2002: Eastern Pacific Hurricanes Jimena of 1991 and Olivia of 1994: The effect of vertical shear on structure and intensity. *Mon. Wea. Rev.*, **130**, 2291–2312, https://doi.org/10.1175/1520-0493(2002)130<2291:EPHJOA>2.0.CO;2.

Boehm, A. M., and M. M. Bell, 2021: Retrieved thermodynamic structure of Hurricane Rita (2005) from airborne multi–Doppler radar data. *J. Atmos. Sci.*, **78**, 1583–1605, https://doi.org/10.1175/JAS-D-20-0195.1.

Bryan, G. H., and J. M. Fritsch, 2002: A benchmark simulation for moist nonhydrostatic numerical models. *Mon. Wea. Rev.*, **130**, 2917–2928, https://doi.org/10.1175/1520-0493(2002)130<2917:ABSFMN>2.0.CO;2.

——, and H. Morrison, 2012: Sensitivity of a simulated squall line to horizontal resolution and parameterization of microphysics. *Mon. Wea. Rev.*, **140**, 202–225, https://doi.org/10.1175/MWR-D-11-00046.1.

Chen, H., and S. G. Gopalakrishnan, 2015: A study on the asymmetric rapid intensification of Hurricane Earl (2010) using the HWRF system. *J. Atmos. Sci.*, **72**, 531–550, https://doi.org/10.1175/JAS-D-14-0097.1.

Chen, S. S., J. A. Knaff, and F. D. Marks Jr., 2006: Effects of vertical wind shear and storm motion on tropical cyclone rainfall asymmetries deduced from TRMM. *Mon. Wea. Rev.*, **134**, 3190–3208, https://doi.org/10.1175/MWR3245.1.

Chen, X., J. A. Zhang, and F. D. Marks, 2019: A thermodynamic pathway leading to rapid intensification of tropical cyclones in shear. *Geophys. Res. Lett.*, **46**, 9241–9251, https://doi.org/10.1029/2019GL083667.

——, J.-F. Gu, J. A. Zhang, F. D. Marks, R. F. Rogers, and J. J. Cione, 2021: Boundary layer recovery and precipitation symmetrization preceding rapid intensification of tropical cyclones under shear. *J. Atmos. Sci.*, **78**, 1523–1544, https://doi.org/10.1175/JAS-D-20-0252.1.

Corbosiero, K. L., and J. Molinari, 2002: The effects of vertical wind shear on the distribution of convection in tropical cyclones. *Mon. Wea. Rev.*, **130**, 2110–2123, https://doi.org/10.1175/1520-0493(2002)130<2110:TEOVWS>2.0.CO;2.

Dai, Y., Q. Li, X. Liu, and L. Wang, 2023: A Lagrangian trajectory analysis of azimuthally asymmetric equivalent potential temperature in the outer core of sheared tropical cyclones. *Adv. Atmos. Sci.*, **40**, 1689–1706, https://doi.org/10.1007/s00376-023-2245-0.

Davis, C., C. Snyder, and A. C. Didlake Jr., 2008: A vortex-based perspective of eastern Pacific tropical cyclone formation. *Mon. Wea. Rev.*, **136**, 2461–2477, https://doi.org/10.1175/2007MWR2317.1.

DeHart, J. C., R. A. Houze Jr., and R. F. Rogers, 2014: Quadrant distribution of tropical cyclone inner-core kinematics in

relation to environmental shear. *J. Atmos. Sci.*, **71**, 2713–2732, https://doi.org/10.1175/JAS-D-13-0298.1.

DeMaria, M., 1996: The effect of vertical shear on tropical cyclone intensity change. *J. Atmos. Sci.*, **53**, 2076–2088, https://doi.org/10.1175/1520-0469(1996)053<2076:TEOVSO>2.0.CO;2.

Didlake, A. C., Jr., and R. A. Houze Jr., 2009: Convective-scale downdrafts in the principal rainband of Hurricane Katrina (2005). *Mon. Wea. Rev.*, **137**, 3269–3293, https://doi.org/10.1175/2009MWR2827.1.

——, and ——, 2013: Dynamics of the stratiform sector of a tropical cyclone rainband. *J. Atmos. Sci.*, **70**, 1891–1911, https://doi.org/10.1175/JAS-D-12-0245.1.

——, P. D. Reasor, R. F. Rogers, and W.-C. Lee, 2018: Dynamics of the transition from spiral rainbands to a secondary eyewall in Hurricane Earl (2010). *J. Atmos. Sci.*, **75**, 2909–2929, https://doi.org/10.1175/JAS-D-17-0348.1.

Donelan, M. A., B. K. Haus, N. Reul, W. J. Plant, M. Stiassnie, H. C. Graber, O. B. Brown, and E. S. Saltzman, 2004: On the limiting aerodynamic roughness of the ocean in very strong winds. *Geophys. Res. Lett.*, **31**, L18306, https://doi.org/10.1029/2004GL019460.

Drennan, W. M., J. A. Zhang, J. R. French, C. McCormick, and P. G. Black, 2007: Turbulent fluxes in the hurricane boundary layer. Part II: Latent heat flux. *J. Atmos. Sci.*, **64**, 1103–1115, https://doi.org/10.1175/JAS3889.1.

Fairall, C. W., E. F. Bradley, J. E. Hare, A. A. Grachev, and J. B. Edson, 2003: Bulk parameterization of air–sea fluxes: Updates and verification for the COARE algorithm. *J. Climate*, **16**, 571–591, https://doi.org/10.1175/1520-0442(2003)016<0571:BPOASF>2.0.CO;2.

Fischer, M. S., P. D. Reasor, R. F. Rogers, and J. F. Gamache, 2022: An analysis of tropical cyclone vortex and convective characteristics in relation to storm intensity using a novel airborne Doppler radar database. *Mon. Wea. Rev.*, **150**, 2255–2278, https://doi.org/10.1175/MWR-D-21-0223.1.

Frank, W. M., and E. A. Ritchie, 2001: Effects of vertical wind shear on the intensity and structure of numerically simulated hurricanes. *Mon. Wea. Rev.*, **129**, 2249–2269, https://doi.org/10.1175/1520-0493(2001)129<2249:EOVWSO>2.0.CO;2.

Gao, S., S. Zhai, B. Chen, and T. Li, 2017: Water budget and intensity change of tropical cyclones over the western North Pacific. *Mon. Wea. Rev.*, **145**, 3009–3023, https://doi.org/10.1175/MWR-D-17-0033.1.

Gopalakrishnan, S. G., K. K. Osuri, F. D. Mark, and U. C. Mohanty, 2019: An inner-core analysis of the axisymmetric and asymmetric intensification of tropical cyclones: Influence of shear. *Mausam*, **70**, 667–690, https://doi.org/10.54302/mausam.v70i4.206.

Gu, J.-F., Z.-M. Tan, and X. Qiu, 2015: Effects of vertical wind shear on inner-core thermodynamics of an idealized simulated tropical cyclone. *J. Atmos. Sci.*, **72**, 511–530, https://doi.org/10.1175/JAS-D-14-0050.1.

——, ——, and ——, 2016: Quadrant-dependent evolution of low-level tangential wind of a tropical cyclone in the shear flow. *J. Atmos. Sci.*, **73**, 1159–1177, https://doi.org/10.1175/JAS-D-15-0165.1.

——, ——, and ——, 2018: The evolution of vortex tilt and vertical motion of tropical cyclones in directional shear flows. *J. Atmos. Sci.*, **75**, 3565–3578, https://doi.org/10.1175/JAS-D-18-0024.1.

——, ——, and ——, 2019: Intensification variability of tropical cyclones in directional shear flows: Vortex tilt–convection coupling. *J. Atmos. Sci.*, **76**, 1827–1844, https://doi.org/10.1175/JAS-D-18-0282.1.

Haynes, P. H., and M. E. McIntyre, 1987: On the evolution of vorticity and potential vorticity in the presence of diabatic heating and frictional or other forces. *J. Atmos. Sci.*, **44**, 828–841, https://doi.org/10.1175/1520-0469(1987)044<0828:OTEOVA>2.0.CO;2.

Hazelton, A. T., R. Rogers, and R. E. Hart, 2015: Shear-relative asymmetries in tropical cyclone eyewall slope. *Mon. Wea. Rev.*, **143**, 883–903, https://doi.org/10.1175/MWR-D-14-00122.1.

Hence, D. A., and R. A. Houze Jr., 2008: Kinematic structure of convective-scale elements in the rainbands of Hurricanes Katrina and Rita (2005). *J. Geophys. Res.*, **113**, D15108, https://doi.org/10.1029/2007JD009429.

Hlywiak, J., and D. S. Nolan, 2022: The evolution of asymmetries in the tropical cyclone boundary layer wind field during landfall. *Mon. Wea. Rev.*, **150**, 529–549, https://doi.org/10.1175/MWR-D-21-0191.1.

Hong, S.-Y., Y. Noh, and J. Dudhia, 2006: A new vertical diffusion package with an explicit treatment of entrainment processes. *Mon. Wea. Rev.*, **134**, 2318–2341, https://doi.org/10.1175/MWR3199.1.

Iacono, M. J., J. S. Delamere, E. J. Mlawer, M. W. Shephard, S. A. Clough, and W. D. Collins, 2008: Radiative forcing by long-lived greenhouse gases: Calculations with the AER radiative transfer models. *J. Geophys. Res.*, **113**, D13103, https://doi.org/10.1029/2008JD009944.

Jones, S. C., 1995: The evolution of vortices in vertical shear. I: Initially barotropic vortices. *Quart. J. Roy. Meteor.*, **121**, 821–851, https://doi.org/10.1002/qj.49712152406.

Kepert, J., 2001: The dynamics of boundary layer jets within the tropical cyclone core. Part I: Linear theory. *J. Atmos. Sci.*, **58**, 2469–2484, https://doi.org/10.1175/1520-0469(2001)058<2469:TDOBLJ>2.0.CO;2.

——, and Y. Wang, 2001: The dynamics of boundary layer jets within the tropical cyclone core. Part II: Nonlinear enhancement. *J. Atmos. Sci.*, **58**, 2485–2501, https://doi.org/10.1175/1520-0469(2001)058<2485:TDOBLJ>2.0.CO;2.

Klotz, B. W., and H. Jiang, 2017: Examination of surface wind asymmetries in tropical cyclones. Part I: General structure and wind shear impacts. *Mon. Wea. Rev.*, **145**, 3989–4009, https://doi.org/10.1175/MWR-D-17-0019.1.

Li, Q., and Y. Dai, 2020: Revisiting azimuthally asymmetric moist instability in the outer core of sheared tropical cyclones. *Mon. Wea. Rev.*, **148**, 1297–1319, https://doi.org/10.1175/MWR-D-19-0004.1.

Ming, J., J. A. Zhang, R. F. Rogers, F. D. Marks, Y. Wang, and N. Cai, 2014: Multiplatform observations of boundary layer structure in the outer rainbands of landfalling typhoons. *J. Geophys. Res. Atmos.*, **119**, 7799–7814, https://doi.org/10.1002/2014JD021637.

——, ——, and ——, 2015: Typhoon kinematic and thermodynamic boundary layer structure from dropsonde composites. *J. Geophys. Res. Atmos.*, **120**, 3158–3172, https://doi.org/10.1002/2014JD022640.

Molinari, J., and D. Vollaro, 2010: Distribution of helicity, CAPE, and shear in tropical cyclones. *J. Atmos. Sci.*, **67**, 274–284, https://doi.org/10.1175/2009JAS3090.1.

——, D. M. Romps, D. Vollaro, and L. Nguyen, 2012: CAPE in tropical cyclones. *J. Atmos. Sci.*, **69**, 2452–2463, https://doi.org/10.1175/JAS-D-11-0254.1.

——, J. Frank, and D. Vollaro, 2013: Convective bursts, downdraft cooling, and boundary layer recovery in a sheared

tropical storm. *Mon. Wea. Rev.*, **141**, 1048–1060, https://doi.org/10.1175/MWR-D-12-00135.1.

Nguyen, L. T., and J. Molinari, 2015: Simulation of the downshear reformation of a tropical cyclone. *J. Atmos. Sci.*, **72**, 4529–4551, https://doi.org/10.1175/JAS-D-15-0036.1.

——, ——, and D. Thomas, 2014: Evaluation of tropical cyclone center identification methods in numerical models. *Mon. Wea. Rev.*, **142**, 4326–4339, https://doi.org/10.1175/MWR-D-14-00044.1.

——, R. F. Rogers, and P. D. Reasor, 2017: Thermodynamic and kinematic influences on precipitation symmetry in sheared tropical cyclones: Bertha and Cristobal (2014). *Mon. Wea. Rev.*, **145**, 4423–4446, https://doi.org/10.1175/MWR-D-17-0073.1.

——, R. Rogers, J. Zawislak, and J. A. Zhang, 2019: Assessing the influence of convective downdrafts and surface enthalpy fluxes on tropical cyclone intensity change in moderate vertical wind shear. *Mon. Wea. Rev.*, **147**, 3519–3534, https://doi.org/10.1175/MWR-D-18-0461.1.

Nolan, D. S., 2011: Evaluating environmental favorableness for tropical cyclone development with the method of point-downscaling. *J. Adv. Model. Earth Syst.*, **3**, M08001, https://doi.org/10.1029/2011MS000063.

Onderlinde, M. J., and D. S. Nolan, 2016: Tropical cyclone–relative environmental helicity and the pathways to intensification in shear. *J. Atmos. Sci.*, **73**, 869–890, https://doi.org/10.1175/JAS-D-15-0261.1.

——, and ——, 2017: The tropical cyclone response to changing wind shear using the method of time-varying point-downscaling. *J. Adv. Model. Earth Syst.*, **9**, 908–931, https://doi.org/10.1002/2016MS000796.

Powell, M. D., 1990: Boundary layer structure and dynamics in outer hurricane rainbands. Part II: Downdraft modification and mixed layer recovery. *Mon. Wea. Rev.*, **118**, 918–938, https://doi.org/10.1175/1520-0493(1990)118<0918:BLSADI>2.0.CO;2.

Raymond, D. J., 1992: Nonlinear balance and potential-vorticity thinking at large Rossby number. *Quart. J. Roy. Meteor. Soc.*, **118**, 987–1015, https://doi.org/10.1002/qj.49711850708.

Reasor, P. D., and M. D. Eastin, 2012: Rapidly intensifying Hurricane Guillermo (1997). Part II: Resilience in shear. *Mon. Wea. Rev.*, **140**, 425–444, https://doi.org/10.1175/MWR-D-11-00080.1.

——, M. T. Montgomery, F. D. Marks Jr., and J. F. Gamache, 2000: Low-wavenumber structure and evolution of the hurricane inner core observed by airborne dual-Doppler radar. *Mon. Wea. Rev.*, **128**, 1653–1680, https://doi.org/10.1175/1520-0493(2000)128<1653:LWSAEO>2.0.CO;2.

——, R. Rogers, and S. Lorsolo, 2013: Environmental flow impacts on tropical cyclone structure diagnosed from airborne Doppler radar composites. *Mon. Wea. Rev.*, **141**, 2949–2969, https://doi.org/10.1175/MWR-D-12-00334.1.

Riemer, M., 2016: Meso-β-scale environment for the stationary band complex of vertically sheared tropical cyclones. *Quart. J. Roy. Meteor. Soc.*, **142**, 2442–2451, https://doi.org/10.1002/qj.2837.

——, M. T. Montgomery, and M. E. Nicholls, 2010: A new paradigm for intensity modification of tropical cyclones: Thermodynamic impact of vertical wind shear on the inflow layer. *Atmos. Chem. Phys.*, **10**, 3163–3188, https://doi.org/10.5194/acp-10-3163-2010.

——, ——, and ——, 2013: Further examination of the thermodynamic modification of the inflow layer of tropical cyclones by vertical wind shear. *Atmos. Chem. Phys.*, **13**, 327–346, https://doi.org/10.5194/acp-13-327-2013.

Rios-Berrios, R., 2020: Impacts of radiation and cold pools on the intensity and vortex tilt of weak tropical cyclones interacting with vertical wind shear. *J. Atmos. Sci.*, **77**, 669–689, https://doi.org/10.1175/JAS-D-19-0159.1.

——, and R. D. Torn, 2017: Climatological analysis of tropical cyclone intensity changes under moderate vertical wind shear. *Mon. Wea. Rev.*, **145**, 1717–1738, https://doi.org/10.1175/MWR-D-16-0350.1.

——, C. A. Davis, and R. D. Torn, 2018: A hypothesis for the intensification of tropical cyclones under moderate vertical wind shear. *J. Atmos. Sci.*, **75**, 4149–4173, https://doi.org/10.1175/JAS-D-18-0070.1.

——, P. M. Finocchio, J. J. Alland, X. Chen, M. S. Fischer, S. N. Stevenson, and D. Tao, 2024: A review of the interactions between tropical cyclones and environmental vertical wind shear. *J. Atmos. Sci.*, **81**, 713–741, https://doi.org/10.1175/JAS-D-23-0022.1.

Rogers, R., P. Reasor, and S. Lorsolo, 2013: Airborne Doppler observations of the inner-core structural differences between intensifying and steady-state tropical cyclones. *Mon. Wea. Rev.*, **141**, 2970–2991, https://doi.org/10.1175/MWR-D-12-00357.1.

Rogers, R. F., P. D. Reasor, and J. A. Zhang, 2015: Multiscale structure and evolution of Hurricane Earl (2010) during rapid intensification. *Mon. Wea. Rev.*, **143**, 536–562, https://doi.org/10.1175/MWR-D-14-00175.1.

Ryglicki, D. R., and R. E. Hart, 2015: An investigation of center-finding techniques for tropical cyclones in mesoscale models. *J. Appl. Meteor. Climatol.*, **54**, 825–846, https://doi.org/10.1175/JAMC-D-14-0106.1.

——, J. D. Doyle, Y. Jin, D. Hodyss, and J. H. Cossuth, 2018: The unexpected rapid intensification of tropical cyclones in moderate vertical wind shear. Part II: Vortex tilt. *Mon. Wea. Rev.*, **146**, 3801–3825, https://doi.org/10.1175/MWR-D-18-0021.1.

Schecter, D. A., 2015: Response of a simulated hurricane to misalignment forcing compared to the predictions of a simple theory. *J. Atmos. Sci.*, **72**, 1235–1260, https://doi.org/10.1175/JAS-D-14-0149.1.

——, 2022: Intensification of tilted tropical cyclones over relatively cool and warm oceans in idealized numerical simulations. *J. Atmos. Sci.*, **79**, 485–512, https://doi.org/10.1175/JAS-D-21-0051.1.

——, and K. Menelaou, 2020: Development of a misaligned tropical cyclone. *J. Atmos. Sci.*, **77**, 79–111, https://doi.org/10.1175/JAS-D-19-0074.1.

Schot, S. H., 1992: Eighty years of Sommerfeld's radiation condition. *Hist. Math.*, **19**, 385–401, https://doi.org/10.1016/0315-0860(92)90004-U.

Shapiro, L. J., 1983: The asymmetric boundary layer flow under a translating hurricane. *J. Atmos. Sci.*, **40**, 1984–1998, https://doi.org/10.1175/1520-0469(1983)040<1984:TABLFU>2.0.CO;2.

Smith, R. K., and M. T. Montgomery, 2015: Toward clarity on understanding tropical cyclone intensification. *J. Atmos. Sci.*, **72**, 3020–3031, https://doi.org/10.1175/JAS-D-15-0017.1.

——, ——, and S. V. Nguyen, 2009: Tropical cyclone spin-up revisited. *Quart. J. Roy. Meteor. Soc.*, **135**, 1321–1335, https://doi.org/10.1002/qj.428.

Sprenger, M., and H. Wernli, 2015: The LAGRANTO Lagrangian analysis tool – version 2.0. *Geosci. Model Dev.*, **8**, 2569–2586, https://doi.org/10.5194/gmd-8-2569-2015.

Tang, B., and K. Emanuel, 2012a: Sensitivity of tropical cyclone intensity to ventilation in an axisymmetric model. *J. Atmos. Sci.*, **69**, 2394–2413, https://doi.org/10.1175/JAS-D-11-0232.1.

——, and ——, 2012b: A ventilation index for tropical cyclones. *Bull. Amer. Meteor. Soc.*, **93**, 1901–1912, https://doi.org/10.1175/BAMS-D-11-00165.1.

Tao, D., and F. Zhang, 2014: Effect of environmental shear, sea-surface temperature, and ambient moisture on the formation and predictability of tropical cyclones: An ensemble-mean perspective. *J. Adv. Model. Earth Syst.*, **6**, 384–404, https://doi.org/10.1002/2014MS000314.

Thomsen, G. L., R. K. Smith, and M. T. Montgomery, 2015: Tropical cyclone flow asymmetries induced by a uniform flow revisited. *J. Adv. Model. Earth Syst.*, **7**, 1265–1284, https://doi.org/10.1002/2015MS000477.

Vico, F., L. Greengard, and M. Ferrando, 2016: Fast convolution with free-space Green's functions. *J. Comput. Phys.*, **323**, 191–203, https://doi.org/10.1016/j.jcp.2016.07.028.

Wadler, J. B., R. F. Rogers, and P. D. Reasor, 2018a: The relationship between spatial variations in the structure of convective bursts and tropical cyclone intensification as determined by airborne Doppler radar. *Mon. Wea. Rev.*, **146**, 761–780, https://doi.org/10.1175/MWR-D-17-0213.1.

——, J. A. Zhang, B. Jaimes, and L. K. Shay, 2018b: Downdrafts and the evolution of boundary layer thermodynamics in Hurricane Earl (2010) before and during rapid intensification. *Mon. Wea. Rev.*, **146**, 3545–3565, https://doi.org/10.1175/MWR-D-18-0090.1.

——, D. S. Nolan, J. A. Zhang, and L. K. Shay, 2021: Thermodynamic characteristics of downdrafts in tropical cyclones as seen in idealized simulations of different intensities. *J. Atmos. Sci.*, **78**, 3503–3524, https://doi.org/10.1175/JAS-D-21-0006.1.

——, J. J. Cione, J. A. Zhang, E. A. Kalina, and J. Kaplan, 2022: The effects of environmental wind shear direction on tropical cyclone boundary layer thermodynamics and intensity change from multiple observational datasets. *Mon. Wea. Rev.*, **150**, 115–134, https://doi.org/10.1175/MWR-D-21-0022.1.

Wang, Y., and G. J. Holland, 1996: Tropical cyclone motion and evolution in vertical shear. *J. Atmos. Sci.*, **53**, 3313–3332, https://doi.org/10.1175/1520-0469(1996)053<3313:TCMAEI>2.0.CO;2.

Wernli, H., and H. C. Davies, 1997: A Lagrangian-based analysis of extratropical cyclones. I: The method and some applications. *Quart. J. Roy. Meteor. Soc.*, **123**, 467–489, https://doi.org/10.1002/qj.49712353811.

Williams, G. J., Jr., 2019: The effects of ice microphysics on the inner core thermal structure of the hurricane boundary layer. *Meteor. Atmos. Phys.*, **131**, 987–1003, https://doi.org/10.1007/s00703-018-0616-3.

——, 2023: Idealized simulations of the boundary layer thermal structure for a landfalling tropical cyclone. *Meteor. Atmos. Phys.*, **135**, 6, https://doi.org/10.1007/s00703-022-00943-0.

Yu, C.-L., A. C. Didlake Jr., F. Zhang, and R. G. Nystrom, 2021: Asymmetric rainband processes leading to secondary eyewall formation in a model simulation of Hurricane Matthew (2016). *J. Atmos. Sci.*, **78**, 29–49, https://doi.org/10.1175/JAS-D-20-0061.1.

——, ——, and ——, 2022: Updraft maintenance and axisymmetrization during secondary eyewall formation in a model simulation of Hurricane Matthew (2016). *J. Atmos. Sci.*, **79**, 1105–1125, https://doi.org/10.1175/JAS-D-21-0103.1.

——, B. Tang, and R. G. Fovell, 2023a: Tropical cyclone tilt and precession in moderate shear: Precession hiatus in a critical shear regime. *J. Atmos. Sci.*, **80**, 909–932, https://doi.org/10.1175/JAS-D-22-0200.1.

——, ——, and ——, 2023b: Diverging behaviors of simulated tropical cyclones in moderate vertical wind shear. *J. Atmos. Sci.*, **80**, 2837–2860, https://doi.org/10.1175/JAS-D-23-0048.1.

Zhang, F., and D. Tao, 2013: Effects of vertical wind shear on the predictability of tropical cyclones. *J. Atmos. Sci.*, **70**, 975–983, https://doi.org/10.1175/JAS-D-12-0133.1.

Zhang, J. A., and R. F. Rogers, 2019: Effects of parameterized boundary layer structure on hurricane rapid intensification in shear. *Mon. Wea. Rev.*, **147**, 853–871, https://doi.org/10.1175/MWR-D-18-0010.1.

——, ——, P. D. Reasor, E. W. Uhlhorn, and F. D. Marks Jr., 2013: Asymmetric hurricane boundary layer structure from dropsonde composites in relation to the environmental vertical wind shear. *Mon. Wea. Rev.*, **141**, 3968–3984, https://doi.org/10.1175/MWR-D-12-00335.1.